PIM Characterization of 3D-printed RF Components

JOSEFIN KARLSSON
MASTER´S THESIS
DEPARTMENT OF ELECTRICAL AND INFORMATION TECHNOLOGY
FACULTY OF ENGINEERING | LTH | LUND UNIVERSITY

PIM Characterization of 3D-printed RF Components

Josefin Karlsson
jo2224ka-s@student.lu.se

Department of Electrical and Information Technology
Lund University

Supervisor: Johan Lundgren & Per Magnusson

Examiner: Daniel Sjöberg

June 12, 2024

Printed in Sweden
Tryckeriet i E-huset, Lund

Abstract

As two signals of different frequencies pass through a nonlinear element, they mix and create unwanted spurious signals. This intermodulation phenomenon is well studied for active components but can also occur from the material in passive components and is then called passive intermodulation (PIM). The PIM energy levels are a concern when designing communication technology, especially satellites, since the PIM signal can drown the information signal.

Concurrently, new manufacture technology is innovated to allow for low waste, free-form fabrication by 3D-printing components in metal. Though advantageous, the intermodulation behavior of the material in 3D-printed metal is unknown, limiting its use in communication system. Therefore, gaining a deeper understanding of PIM behavior in 3D-printed components is essential to fully harness the potential of 3D-printing technology.

The thesis investigates how the PIM-performance of radio frequency (RF) parts manufactured by metal 3D-printing compare to standard subtractive manufacture milling technology. An X-band test setup is designed, including a coaxial rectangular waveguide with a 3D-printed metal sample as the test object. The applied power is varied and the corresponding PIM level is measured. The same test is performed with a milled test sample. The results are compared and conclude that 3D-printed samples on average perform 5 dB worse than milled samples. Within the industry, this degradation is deemed acceptable when accounting for the other benefits the manufacture method intel. This result supports the theory that there is a connection between the porosity of a material and the PIM level it induces. Overall, the test setup was designed successfully and the PIM levels of 3D-printed RF components could be measured and characterized. Future research within the field is however crucial to deepen our understanding. By continuing to explore these areas, the potential for improving the reliability and performance of AM-SLM printed components in electromagnetic applications can be significantly enhanced.

Keywords: Intermodulation distortion, passive intermodulation, nonlinear analysis, additive manufacturing, AM-SLM, surface roughness, electrical conductivity

Populärvetenskaplig Sammanfattning

I dagens globala samhälle finns en växande efterfrågan på trådlös kommunikation. För att möta denna efterfrågan behöver kommunikationssystemen utvecklas, till exempel genom att använda högre frekvenser som i 5G, öka antalet användare som kan använda systemet samtidigt eller använda större antennsystem. Detta ökar dock risken för störningar mellan användares kommunikationslänkar, vilket leder till sämre prestanda.

När två signaler med olika frekvenser går igenom en icke-linjär elektronisk komponent, blandas de och skapar nya signaler, vilket kallas intermodulation. Problem uppstår när den blandade signalen hamnar i ett mottagarband, likt hur ljud från andra samtal kan störa ett samtal i ett fullsatt rum. Intermodulation har studerats mycket för aktiva komponenter som transistorer och integrerade kretsar, som behöver ström för att fungera och kan förstärka signaler. Men intermodulation kan också ske i passiva komponenter, som inte behöver ström. När detta händer på grund av materialets egenskaper kallas det PIM (Passiv Intermodulation).

Nya tillverkningsteknologier som 3D-printing av metall möjliggör mindre restprodukter och friare geometrier. Trots många fördelar är intermodulationsbeteendet hos 3D-printad metall okänt, vilket begränsar användningen inom kommunikationssystem. Därför är en djupare förståelse av PIM i 3D-printade komponenter viktig.

Denna avhandling undersöker hur PIM-prestandan hos RF-komponenter påverkas av 3D-printing jämfört med traditionella metoder som svarvning. En testuppställning för höga frekvenser designades, där metallprover skapades med både 3D-printning och fräsning. Resultaten visar att 3D-printade prover presterade i snitt 5 dB sämre än frästa prover, vilket anses acceptabelt inom industrin för de fördelar som 3D-printning ger. Projektet skapade en framgångsrik testuppställning och resultaten visar en lovande start för 3D-printning av elektromagnetiska RF-komponenter. Vidare forskning behövs för att säkerställa resultaten och göra 3D-printning tillämpbar inom satellit- och mobilindustrin.

Acknowledgement

My sincere thanks to Beyond Gravity for the opportunity to conduct my thesis work with them. It has been an invaluable learning experience. I am deeply thankful to my supervisor, Per Magnusson for the support, teachings and kindness. Thanks to you I leave a better, even more curious engineer. I would also like to thank my supervisor, Johan Lundgren, for your helpful guidance throughout the process.

A special thanks to the people at the Department of Microtechnology and Nanoscience at Chalmers University for their collaboration and our brainstorming sessions, which have made this project both enjoyable and rewarding.

Lastly I would like to extend my most profound and heartfelt thanks to all my teachers through the years. No one mentioned and no one forgotten.

Table of Contents

Acronyms

3D	Three Dimension
AM	Additive Manufacturing
BPF	Band Pass Filter
DUT	Device Under Test
HFSS	High Frequency Simulation Software
HPF	High Pass Filter
IM3	Third Order Intermodulation
IMD	Intermodulation Distortion
LNA	Low Noise Amplifier
MM	Metal-Metal
MIM	Metal–Insulator–Metal
PIM	Passive Intermodulation
RF	Radio Frequency
RX	Receiver
WR	Rectangular Waveguide
SEM	Scanning Electron Microscope
SNR	Signal-to-Noise Ratio
S-parameters	Scattering Parameters
SLM	Selective Laser Melting
TE	Transverse Electric
TEM	Transverse Electromagnetic
TM	Transverse Magnetic
TWT	Traveling Wave Tube
TX	Transmitter
VNA	Vector Network Analyser

List of Figures

List of Tables

Chapter 1
Introduction

In today's global society, communication is vital. Whether it is exchanging ideas between colleagues in different continents, connecting with loved ones across oceans, or collaborating with international partners on projects, effective communication bridges the geographical gaps that separate us. According to Ericsson mobility report from 2023, the mobile network data traffic growth between 2022 and 2023 was around 7 % [4]. Further, the Ericsson mobility report continues to account for a strong uptake of 5G, with around 600 million new subscriptions added globally during 2023, showing that demand for high-performance connectivity remains. To meet the rising demand, wireless communication capacity must expand, indicating a need of higher frequencies, bandwidths, input powers, and the coexistence of multiple users [5]. This elevates the risk of interference among communication systems, ultimately degrading system performance [6].

Various forms of interference exist. This thesis focuses on passive unwanted spurious signals, a phenomenon known as passive intermodulation (PIM). Intermodulation is the combination of two or more input signals as a device interacts with a nonlinear element, which results in several overtones and harmonics [7]. By filtering, the majority of these can be removed before the antenna. However, to completely remove all PIM products, the filter would have to be at the very end of the transmitting chain, which is not possible since that is where the antenna is located. Hence, if the antenna is for example 3D-printed, the PIM products from it would transmit through. Typically, the received signal is very weak. Especially in satellite communication since it has travelled for a long distance. The received signals therefore risk being drowned in the inherent PIM products within the antenna system itself, as the received signals will have power levels similar to the power levels of the PIM products

Though nonlinear behavior has been studied, focus has been given to active devices and little attention has been paid to passive intermodulation. This is primarily due to the low power in PIM signals and the challenge in modeling passive structures. Passive structures demonstrate non-ideal behavior due to factors such as parasitic elements, temperature sensitivity, and manufacturing tolerances [8, 9]. These deviations from ideal performance differ from one component to another, making accurate modeling challenging. In addition, multiple sources within the same system can generate PIM, making it difficult to find the source. However, in satellite systems, PIM is of significant concern, due to the high transmitting power and the vulnerability of satellite receivers [5]. In certain cases, the PIM require-

ments can be as stringent as −140 dBm [10]. This stringent standard showcases how critically important PIM performance is within the industry, as even minor deviations can significantly impact the quality and reliability of communication systems. Consequently, a considerable amount of research on PIM is directed towards addressing the specific challenges faced by satellite communication systems [11].

Methods of avoiding PIM are applied when designing satellite systems and other high power equipment. A key factor in the design is to avoid metal-to-metal contacts, unless high pressure can be applied in the joints between the metal parts [12]. 3D-printing of metal parts, also known as additional manufacturing (AM), is becoming more attractive as the method opens up the potential for new geometries not feasible for standard mechanical machining methods [13]. However, the 3D-printing process could introduce new sources of PIM, as it continuously melts small grains of metal together when building the part, limiting its usage for communication systems. Therefore, more research is needed to evaluate the usage of additive manufacture methods for communication systems. This thesis aim to investigate this aspect.

1.1 Project Aim

The aim of this thesis project is to investigate how the PIM-performance of metal Radio Frequency (RF) parts is affected by metal 3D-printing, also known as Additive Manufacture - Selective Laser Melting (AM-SLM). This investigation entails the development of test objects engineered to likely induce PIM signals by inducing high surface currents and manufactures them using both metal 3D-printing techniques and standard subtractive manufacturing milling technology. Further, the project includes designing an experimental setup and performing tests to examine and measure passive intermodulation effects.

The goal is to design a test object to induce PIM, as well as design an X-band test setup, to measure and analyze differences in PIM characteristics. The main challenges include designing a test object with high enough surface currents to elicit PIM responses, as well as designing an appropriate test setup which in itself does not contribute considerable levels of PIM to the final measurements.

This research serves a dual purpose: to explore the impact of the AM-SLM manufacture method on signal quality, and to deepen the understanding of PIM, laying some groundwork for future research and inspiring further advancements in the field of digital communication.

1.2 Related Work

Previous investigations have been made which indicated that metal-to-metal connections induce PIM, *e.g.* in waveguides [14], [15], cable connectors [16], [17], duplexers [18] and transmission lines [9], [19]. Further, research indicates that the surface roughness of AM-SLM material is close to 2000 % larger than that of milled aluminum [20]. Research further suggests the AM-SLM method results in a higher porosity, which would increase the PIM effects compared to standard subtractive

manufacturing milling technology [21]. Similar conclusions are reached in another study, which proposes that the softness, also known as the porosity, of the surfaces and the mechanical properties of the contacting metals are important for the PIM generation [14]. Therefore this research aims to examine and compare the PIM characterization of an unprocessed printed AM-SLM sample, which should have a high porosity and surface roughness, and a milled sample, which should have a lower porosity and surface roughness.

1.3 Methodology

To investigate PIM characterization of 3D-printed RF components, the project commences with an extensive literature study on the subject, along with a summary of current knowledge within the fields of intermodulation, AM-SLM technology and RF design to deepen understanding and provide context. Thereafter, a setup for PIM-measurements, as well as test objects, are designed and then translated into component-form using previous work from the literature study as a base. The setup and test objects were based on consultations with lead specialist in RF design Per Magnusson at Beyond Gravity, as well as input from the Department of Microtechnology and Nanoscience at Chalmers University. A specially designed RF shielded anechoic chambers was available to cater PIM measurements. Consideration was given to the availability of components in the laboratories at Beyond Gravity and additional equipment were designed. Finally, the setup was implemented and measurements of PIM could then be recorded and analyzed.

1.3.1 Limitations

The experimental design was constrained by the availability of three test object of each material and post processing for analysis. Effort was made to ensure the accuracy and validity of the measurements, but the reliance on a few test object raises an uncertainty in the reliability and credibility of the results. The printed components are limited to the metal printing quality provided by Research Institutes of Sweden (RISE). It is possible to achieve a denser structure, but the manufacture method for the tested samples is deemed industry standard. Further, the setup is limited by the available equipment on site. The setup is by itself prone to generating PIM, but is deemed to be sufficient for accurate results by the aid of proficient filters. These limitations should be taken into consideration when interpreting and applying the outcomes of the study.

1.4 Thesis Structure

The rest of the thesis is organized as follows:

- **Fundamentals of Nonlinear Distortion** - This chapter outlines the fundamentals of intermodulation distortion. The chapter describes how nonlinear devices generate new frequency content. Additionally, some sources of passive intermodulation are described and how it ties to the material properties.

- **Fundamentals of AM-SLM** - This chapter provides a background to AM-SLM and how it can be utilized. The AM-SLM process and parameters are explained, as well as Hot Isostatic Pressure (HIP) Post Processing.
- **PIM Testing: Setup and Component Design** - This chapter introduces the test setup, motivates the choice of equipment and provides details about the designed components.
- **Characterization of PIM in AM-SLM RF Components** - In this chapter, the simulation and measurement setup configurations are described. The experimental results of the AM-SLM sample is compared to the milled and HIP post processed ones.
- **Conclusion and Future Directions** - Finally, this chapter concludes the work and discuss future studies within the field.

Chapter 2

Fundamentals of Nonlinear Distortion

This chapter presents fundamental theory of nonlinear distortion. Section 2.1 provides a mathematical description of how new frequency components are generated through nonlinear phenomenon. Section 2.2 goes into detail on passive intermodulation distortion and its sources. Lastly, Section 2.3 covers the Groiss model, tying surface roughness, skin depth, and conduction losses together.

2.1 Intermodulation Distortion

In today's wireless communication systems, the Signal-to-Noise Ratio (SNR) is a key measure of the signal quality [22]. Interference of all types degrade the SNR of a system. Intermodulation Distortion (IMD) is a type of nonlinear distortion that occurs in electronic systems when multiple signals of different frequencies pass through a nonlinear device or system [5]. This results in the generation of new frequency components, known as intermodulation products, at frequencies that are the sum and difference of the original signal frequencies and their harmonics. These new frequencies are a combination of the linear and nonlinear components between them [23]. Consider a sinusoidal input signal with frequency $f_1 = \omega_1/2\pi$, described as $x(t) = A\cos(\omega_1 t)$. A is the amplitude of the signal and the output of the nonlinear system is obtained by Taylor expansion

$$y(t) = \sum_{n=1}^{\infty} a_1 x(t) + a_2 x^2(t) + a_3 x^3(t) + \cdots + a_n x^n(t) \tag{2.1}$$

where a_n is the n^{th}-order Taylor coefficient, determined around a point t_0 and calculated by

$$a_n = \frac{1}{n!}\frac{d^n y(t_0)}{dx^n} \tag{2.2}$$

Thereby, the output signal is

$$\begin{aligned} y(t) = \frac{1}{2}a_2 A^2 + \left(a_1 A + \frac{3}{4}a_3 A^3\right)\cos(\omega_1 t) \\ + \frac{1}{2}a_2 A^2 \cos(2\omega_1 t) + \frac{1}{4}a_3 A^3 \cos(3\omega_1 t) + \ldots \end{aligned} \tag{2.3}$$

Studying (2.3), the results show that a single input excitation generates multiple signals, where A is a scaling factor which determines the amplitude of the signal.

The same principle is applicable for a source of two sinusoidal signals. Let the signals have the same amplitude A and frequency components $f_1 = \omega_1/2\pi$ and $f_2 = \omega_2/2\pi$. The signal is then $x(t) = A\cos(\omega_1 t) + A\cos(\omega_2 t)$ with the output signal as

$$\begin{aligned} y(t) = a_2A^2 &+ \left(a_1A + \frac{9}{4}a_3A^3\right)\cos(\omega_{1,2}t) \\ &+ \frac{1}{2}a_2A^2\cos(2\omega_{1,2}t) + \frac{1}{4}a_3A^3\cos(3\omega_{1,2}t) \\ &+ a_2A^2\cos(\omega_1 \pm \omega_2 t) + \frac{3}{4}a_3A^3\cos(2\omega_{1,2} \pm \omega_{2,1}t) \end{aligned} \tag{2.4}$$

Studying (2.4), the Taylor expansion generates the same time-varying amplitude and harmonics as (2.3), but also a set of signals with mixed frequency components from ω_1 and ω_2. The expression $\omega_{1,2} \pm \omega_{2,1}$ indicates four combinations in total, namely $\omega_1 + \omega_2$, $\omega_1 - \omega_2$, $\omega_2 + \omega_1$, and $\omega_2 - \omega_1$. These new signals are called intermodulation products [7]. The order of the intermodulation product is determined by the combination of the original signal frequencies that produce it. In a system with two input signals f_1 and f_2, the order of the intermodulation products is categorized based on the mathematical relationship between their frequencies [22]. For example, studying (2.4), the second order intermodulation is represented in the term $a_2A^2\cos(\omega_1 \pm \omega_2 t)$ and is generated when the original signals combine as $f_1 \pm f_2$. Similarly, the third order intermodulation product is represented in the term $\frac{3}{4}a_3A^3\cos(2\omega_{1,2} \pm \omega_{2,1}t)$ as $2f_1 - f_2$ and $2f_2 - f_1$. This illustrates the pattern that the intermodulation signals are generated when the original signals combine at the sum and difference frequencies of the original signals and their harmonics ($mf_1 \pm nf_2$), where m and n are integers representing harmonic multiples of the original frequencies. Higher-order intermodulation products involve combinations of higher-order harmonics of the original signals and become increasingly complex as the order increases.

It is also interesting to note that a nonlinearity is necessary for the harmonic distortion to occur. This can be understood by studying (2.3) and (2.4). If all derivatives with an order higher than one is zero, then (2.2) is zero. This would mean (2.3) would equal $y(t) = a_1A\cos(\omega t)$ and (2.4) would equal $y(t) = a_1A\cos(\omega_{1,2}t)$. There is therefore a need for a nonlinearity, hence for derivatives of higher order, for harmonic distortion and intermodulation to occur.

The two signals can mix and produce third-order, fifth-order, seventh-order and higher-order harmonic signal products. The challenge with these harmonics is that they may appear in the frequency spectra of either the transmitting antenna or in other receiving systems aboard the satellite. In such cases, the PIM signal poses a risk of overpowering the weaker signal received from a distant transmitter. Among these intermodulation products, the third-order intermodulation (IM3) is often the most critical in practical applications, especially in RF communication systems, as it exhibits the highest power levels. This is because the amplitude of

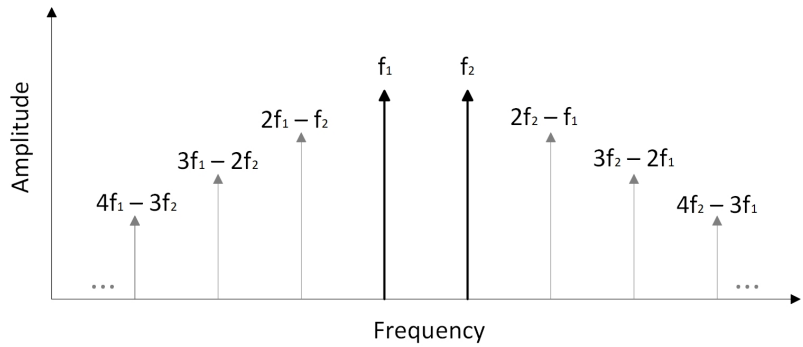

Figure 2.1: The intermodulation frequency spectrum around the fundamental frequencies f_1 and f_2.

intermodulation distortion decreases with increasing order [22]. In Figure 2.1, only the odd intermodulation products are depicted, although there are intermodulation products of even orders as well.

Up until now, only two signals were considered, serving as a brief introduction to the area. However, in real-world applications the signal is carried on a bandwidth consisting of a span of frequencies. The different frequency components are affected, bent and reflected differently, causing dispersion [24]. Additionally, a real world mobile communication system carry multiple users at all times. Each user introduces its own signal with its unique frequency characteristics, modulation schemes, and data rates. As a result, the frequency spectrum becomes crowded, with multiple signals occupying different frequency bands. In summary, in real-world applications are more complex then the previously discussed two signal system and require more filtering, modulation schemes and overall consideration.

2.2 Passive Intermodulation Distortion

Research within intermodulation distortion often focus on active devices which are known to be inherently nonlinear. However, the same phenomena where several signals pass through a nonlinear element and mix can occur in passive devices as well [5]. This is called PIM distortion and when the PIM level is higher than the noise floor of the system, it can significantly reduce the SNR at the receiver [25]. Unlike active intermodulation it primarily stems from nonlinearities within passive components, notably those found in connectors, cables, and antennas [26, 16, 18]. In ideal conditions these components are linear, though passive components can exhibit nonlinear behavior due to factors such as metal-to-metal junctions, surface imperfections or contaminants. Under high input powers levels these factors are known to generate PIM [24].

PIM is a critical concern within satellite communication systems since they carry highly sensitive transmitters and receivers, while they at the same time transmit high power [10], [11]. To provide a perspective, a base station has a typical PIM requirement level of -150 dBc, dependent upon the modulation technique

[27]. Here, dBc stands for decibels relative to the carrier, a unit of measurement used to quantify the level of a signal or noise relative to the carrier signal level. −150 dBc means the signal power is 150 decibels below the power level of the carrier signal. In satellite communications the impact of PIM is deemed even more serious with a PIM requirement level that spans from −175 dBc to −200 dBc [28]. Under static conditions, the PIM performance meet the required standards. However, during the launch of satellite systems, mechanical stresses and vibrations affect connectors, cables, and antennas. These dynamic conditions can significantly increase PIM disturbances, leading to a decrease in SNR [29] This highlights the importance of a low value PIM and high value SNR in satellite systems.

2.2.1 Sources for Passive Intermodulation

The sources of PIM can typically be divided into two types: contact nonlinearity and material nonlinearity [22]. The first type refers to any kind of metallic contacts and the second to material properties and the internal electric fields.

Metallic Contacts

When current flows through a metallic contact it is known to generate nonlinear behavior [5]. Metallic contacts are essential in most electrical appliances, therefore this kind of PIM generator has been studied, *e.g.* in cable connectors [16], [17], transmission lines [9], [19] and duplexers [18]. Generally, due to surface roughness the contact area is merely a fraction of the total area as shown in Fig. 2.2. As illustrated, metal-metal (MM) contacts are created in between the metal layers and metal-isolator-metal (MIM) contacts are created with the air cavities as isolators. This pattern of multiple MM contact points is what is known to genereate PIM. To minimize multiple points of contact, it is desirable to induce high pressure between the interfaces, effectively forcing them together [14].

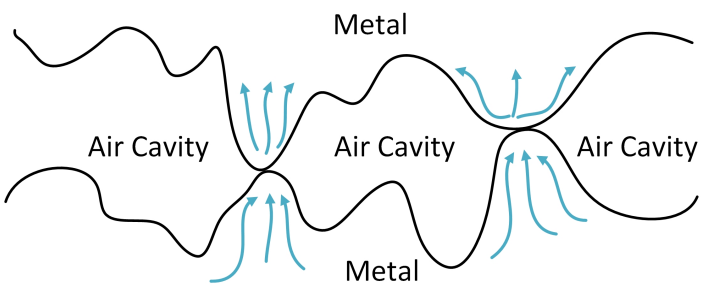

Figure 2.2: Illustration of the rough surface contact between two metals, creating MM and MIM contacts.

The type of nonlinearity depends on the kind of contact, if it is MM or MIM [5]. In [14], PIM generation between two metallic waveguide flanges was studied. The studies concluded that in the void region, the MIM contact is susceptible to generate PIM through tunneling or thermionic emission. Meanwhile, in the

MM contact zones, the PIM is generated by the change of current direction which creates a constriction resistance.

Material Properties

Material nonlinearity refers to material characterized by a nonlinear current response due to an applied voltage. This type of behavior may be associated to conductive, dielectric, or magnetic properties of materials [22]. Cracks or gaps can introduce discontinuities in the electromagnetic field, causing localized regions of high electrical field intensity [24]. When RF signals pass through these areas, nonlinear effects such as micro-arcing, metal migration, or electron tunneling can occur, leading to the creation of PIM [30]. This will be further discussed in the following section.

2.3 Surface Roughness Model

Material properties of RF components are shown to impact the PIM performance [5, 31, 32]. When the applied pressure between two surfaces is high, it follows that the main source of intermodulation occurs in the MIM regions since many contact zones are created. Therefore, the primary source of PIM in high pressure areas include processes such as surface roughness, tunneling, and thermionic emission [5, 14]. These mechanisms therefore contribute to the generation of unwanted intermodulation products in the system.

From Section 2.2.1, it becomes evident that multiple points of contact, stemming from surface roughness disrupts the flow of electric current, leading to an increase in conductor losses. Different models for calculating the attenuation in a conductor due to surface roughness exist [33]. One is Morgan-Hammerstad, which has low complexity and is therefore more intuitive, however the model is only accurate for frequencies up to 4 GHz [31]. A modified version is the Groiss model, which perform accurately up to 12 GHz [32]. The Groiss model refers to a computational approach for analyzing lossy cavity resonators, such as MIM contacts, using the finite element method (FEM). It demonstrates that the losses of an RF component correlate with both surface roughness (R_{rms}) and skin depth (δ).

2.3.1 Skin depth

The skin depth refers to the depth at which the amplitude of an electromagnetic wave's electric or magnetic field decreases to about 37 % of its surface value as it penetrates a conducting medium [20]. 37 % corresponds to the factor $1/e$ and beyond this depth, the current density decreases rapidly. It is a key factor in surface roughness models and is formulated as

$$\delta = \sqrt{\frac{1}{\pi f_0 \mu \sigma}} \tag{2.5}$$

where μ is the magnetic permeability of free space, $\mu = \mu_0 = 4\pi \times 10^{-7}$ H/m for most metals, including aluminum, and is therefore used in this study. σ is

the electrical conductivity. The expression is valid for high frequencies in the RF range.

When a resonator is excited by an aperture-coupled waveguide, the problem can be approached as a closed cavity with absorbing boundary conditions. The solution involves computing the eigen resonance. It is assumed that the resonator is excited and then oscillates freely. If both the dielectric and the walls are ideal, the amplitude of the field remains constant over time. However, in the presence of losses, it decays over time as

$$\mathbf{E} = \mathbf{E}_0 e^{(-\omega_\mathrm{i} + \mathrm{j}\omega_\mathrm{r})t} = \mathbf{E}_0 e^{\mathrm{j}\omega_c t} \tag{2.6}$$

where $\mathbf{E}_0$ is the field at $t = 0$ and ω_c is the complex frequency. ω_r is the real eigen-frequency representing the oscillation, while ω_i is the the imaginary part represents the rate at which the oscillations decay due to damping.

According to the Groiss' model referenced in [32], the lossy field depend on the surface admittance Y_s, which can be expressed as

$$Y_\mathrm{s} = \frac{(1-\mathrm{j})}{C_\mathrm{s}} \sqrt{\frac{\sigma_\mathrm{s}}{2\omega_\mathrm{c}\mu}} \tag{2.7}$$

where σ_s is the conductivity of the walls. C_s is a factor that takes the surface roughness into account, as shown in [32]

$$C_\mathrm{s} = 1 + e^{-\left(\frac{\delta}{2\mathrm{h}}\right)^{1.6}} \tag{2.8}$$

where h is the surface roughness. It is measured as the root mean square peak-to-valley distance. Simplified, this means it is measured as the average distance between the depth of the valleys to the height of the peaks. Eq. (2.8) show that the surface admittance of the walls within a structure depend on the roughness of the surface and the skin depth. If h has a large value relative to δ, meaning the surface is rough compared to the skin depth, then the value of C_s approach 2. If h is small compared to δ, meaning the surface is smooth compared to the skin depth, then C_s approach 1. This indicates that for a rough surface, Y_s is half as large as it is for a smooth surface. The admittance is lower if the surface is rough, which is logical as the admittance is a measure of how easily the current can flow. As the surface admittance decreases, the losses increase in those areas as well which could imply the underlying cause for an increase in PIM.

2.3.2 Relationship Between Electrical Conductivity and Porosity

Electrical conductivity is tied to the porosity of the material [34]. A high presence of pores creates a discontinuity in the metal structure, which impedes the flow of electrical current. This indicates that the resistivity of a material increases as the number of pores increases. Further, in [34] it is stated that pore size, shape, and distribution impact the electrical conductivity, provided it is whin the skindepth or region where current flows. Material with smaller, more uniformly distributed pores may exhibit a higher electrical conductivity compared to materials with larger, irregularly shaped pores.

In summary, materials with higher porosity tend to have a lower electrical conductivity compared to dense materials with fewer or no pores. To tie back to presence of PIM, a material with higher porosity has a higher skin effect. The skin effect is in turn correlated to the impedance in the material. Hence, a higher impedance indicates a higher likelihood of PIM.

Chapter 3
Fundamentals of AM-SLM

This chapter presents the fundamental theory of Additive Manufacturing-Selective Laser Melting (AM-SLM), also known as metal 3D-printing. Section 3.1 provides an overview on additive manufacture technologies, its history and areas of application. Section 3.2 explains the methodology and build considerations behind Selective Laser Melting. Thereafter, Section 3.3 explains why AM-SLM might result in PIM generation. Lastly, in Section 3.4 provide insight in a post-processing method called Hot Isostatic Pressure, which might be an interesting method to use for further research within the field.

3.1 Overview on Additive Manufacturing Technologies

Any manufacturing technique can be classed as either subtractive, formative or additive [35]. Consequently, each existing technique either falls completely into one of these categories, or is a hybrid between them. Additive manufacturing (AM) is becoming increasingly popular across industries with sales of AM systems for metal parts increased by 27.2 % in 2022 [36]. AM has applications across various industries, including healthcare [37, 38], automotive [39] and aerospace [40]. In recent years, AM technologies have extended into the RF field, producing a new generation of microwave and millimeter-wave devices [41, 42]. Further, AM technologies are becoming increasingly popular within the satellite industry since it holds promise for reducing waste and lead time, effectively reducing costs [43]. Additionally, the additive method can build parts not possible with subtractive manufacturing processes since it allows for freeform fabrication of geometrically complex parts without special fixtures as required in material removal processes [35]. One example on such a fixture can be seen in Fig. 3.1, where circularly polarized array antenna has been AM-SLM printed. Attached to one of the openings is a milled horn antenna. The difference in the surface roughness between the shiny milled horn and the matte printed array antenna is visible.

Since the late 1980s, AM technologies have been a subject of research and today, AM solutions are more reliable and effective than ever before [43]. The American Society of Testing and Materials (ASTM) classify AM technologies into several categories, as listed in Table. 3.1. The processes are divided into binder jetting, direct energy deposition, material extrusion, material jetting, powder bed fusion, sheet lamination, and vat photopolymerization [3]. Though each process

Figure 3.1: AM-SLM printed circularly polarized array antenna with a milled horn attached.

has their unique technology, they all share the principle of additive manufacturing where 3D-parts are fabricated directly from CAD models and built in a layer-by-layer manner. Also noticeable in Table. 3.1 is the materials, ranging from metal to wax, showcasing the technologies wide range of application areas.

3.2 Process of Selective Laser Melting

One example of AM methods being employed withing the satellite industry is a project RUAG Space did in collaboration with Altair ProductDesign, where a 40 cm long antenna bracket was developed [44]. Another example is Airbus Defence and Space, which developed an antenna bracket in titanium alloy [45]. Both were deemed successfully. Certain of the techniques in Table. 3.1 are especially investigated for satellite applications, like material extrusion, material jetting, vat photopolymerization, and powder-bed fusion. Powder bed fusion will now be further discussed, with focus on one of the commonly used methods: Selective Laser Melting (SLM).

SLM melts the metal powder with a high-power laser beam to form a metallic part as illustrated in Fig. 3.2a [46]. The process starts with a CAD file, where generated support structures for overhanging features is added to the design before conversion to a STL file [43]. Before building, a thin layer of metal powder is laid on the substrate plate within the building chamber [46]. The high-energy density laser is used to fuse areas of the metal powder according to the processed data.

Table 3.1: American Society for Testing and Materials classification of additive manufacture technology [3].

Process	Technology	Materials
Binder Jetting	3D printing Ink-jetting S-print M-print	Metal Polymer Ceramic
Direct Energy Deposition	Direct Metal Deposition Laser Deposition Laser Consolidation Electron Beam Direct Melting	Metal
Material Extrusion	Fused Deposition Modeling	Polymer
Material Jetting	Polyjet Ink-jetting Thermojet	Photopolymer Wax
Powder Bed Fusion	Selective Laser Sintering Selective Laser Melting Electron Beam Melting	Metal Polymer Ceramic
Sheet Lamination	Ultrasonic Consolidation Laminated Object Manufacture	Hybrids Metallic Ceramic
Vat Photopolymerization	Stereolithography Digital Light Processing	Photopolymer Ceramic

The high-power laser enables full melting of the powders, making the fabricated component exhibit a density close to the theoretical density. Theoretical density means the maximum possible density that the material could achieve under ideal conditions, such as zero defects, impurities, or structural imperfections present in real-world materials. The built component are therefore of similar characteristics as a milled equivalent. The building platform is lowered after each layer is scanned, see Fig. 3.2b. A new layer of metal powder is deposited on top of the precious layer with help of a roller. This process is repeated until the entire component is completed. As the component is being built, it is lowered into the powder bed and therefore relieved from the force of gravity to bend or alter horizontal or hanging structures until it is extracted from the powder bed.

3.2.1 Parameters to Consider in SLM

In the selective laser melting (SLM) process, various parameters, including the type of laser radiation source, atmosphere control, temperature within the chamber, properties of the powder used, and process parameters such as laser power, layer thickness, and scanning strategy, significantly influence the quality and properties of the fabricated components [47]. These parameters play crucial roles in

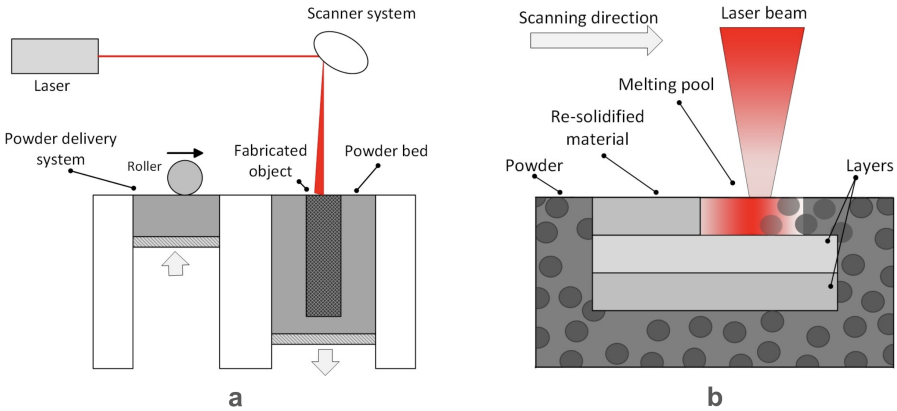

Figure 3.2: Illustrations of the SLM process. **a**. Schematic overview of SLM cycle. **b**. Detailed view of the SLM process, referring to the three different material states: powder, molten pool, and re-solidified material.

determining material characteristics, build quality, and construction time. To summarize, a successful SLM fabrication requires careful consideration and optimization of these parameters.

In [47], some important parameters for the SLM process are discussed. It states that the type of laser radiation source is crucial due to its varied energy absorption parameters for different materials, which are dependent on the wavelength of the laser source. Further, the atmosphere in the processing chamber plays a vital role in preventing oxidation and ensuring proper material properties. The research in [47] also show that the temperature control within the chamber, typically set between room temperature and 300°C, affects the flow of metal grains and melting behavior of metal powders. The large energy input to melt the grains can cause problems such as balling, residual stress and part deformation. Moreover, the properties of the powder used, including grain size and shape, significantly impact the feasibility of the SLM process and the quality of the final product. Altering these parameters are necessary to achieve optimal fabrication outcomes.

3.2.2 Stair-Stepping Effect in Layered Manufacturing

One important aspect to consider is part orientation during the printing session. Since the slicing process generate a series of horizontal cross sections build up stacked on one another, the CAD geometry might not precisely conform in the vertical plane (*i.e*, in the Z-direction) [48]. An example of three important considerations are provided in Fig. 3.3. All images shows the "stair-stepping" phenomenon. The first image (Fig. 3.3a) shows three different ways in which the layers might conform to the CAD geometry to illustrate the importance of where the layers are centered. Example (i) demonstrates how the geometry is shaped from the top down, while (ii) illustrates the opposite build direction. In both cases, build-

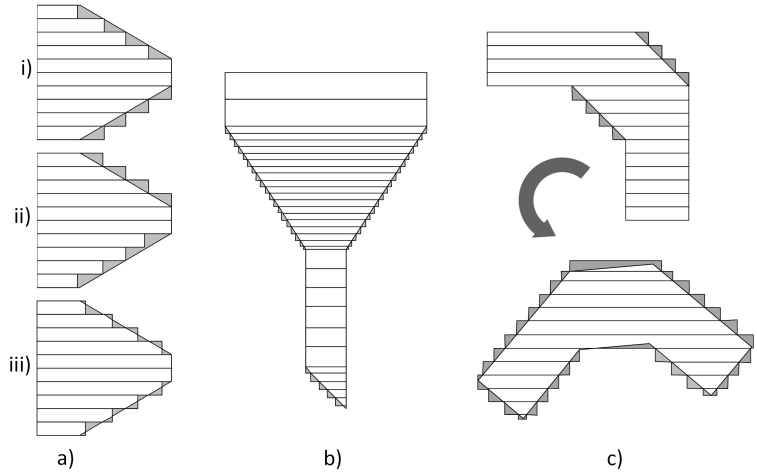

Figure 3.3: Illustration of the stair-stepping phenomenon. **a**. Effect of layer centering. **b**. Adjusted layer thickness. **c**. Importance of part orientation.

ing over a slope results in the stair-stepping effect, causing some deviation from the original CAD design. The severity of this deviation is influenced by the slope gradient. In scenario (ii), additional processing power is required to correct the data and ensure that only positive deviations are permitted for all layers. Lastly, scenario (iii) represents an intermediate situation where each layer's center closely aligns with the CAD geometry. Although this approach optimizes the design by minimizing deviations in both directions, it also leads to longer processing times due to the need for calculating additional data corrections in both directions. To address the problem, it is common to opt for a overhanging design, using slightly more material, which can then be removed during post-processing [40]. However, considering one of the main benefits of additive manufacturing is the possibility to produce complex geometries as stated in [35]. Therefore, one cannot always count on post-processing being an option. There is a trade off between the accessibility of geometries in additive manufacturing and the accuracy of the geometry itself, at the cost of data processing.

Another strategy to enhance the process involves adjusting the layer thickness throughout the design. Thinner layers result in smoother conformity to the design. However, employing thin layers uniformly would significantly increase processing time. Instead, layer thickness can be varied throughout the design, as depicted in Fig. 3.3b. Thinner layers are applied in areas where the stair-stepping effect has a more pronounced effect, hence in the areas of steep slopes.

Lastly, the orientation of the printed part must be carefully considered. While surfaces parallel to the horizontal build plane do not exhibit the stair-stepping effect, all other surfaces do. Therefore, it is advisable to orient parts such that visually critical faces are built horizontally, where important dimensions align with the slice axis. However, selecting the optimal part orientation is not solely based

on minimizing height. As shown in Fig. 3.3c, factors such as centering and layer thickness variation also play a crucial role and must be taken into account. The piece experienced less of the step effect before it was rotated to the lowest position.

3.3 AM-SLM Build and Concerns for PIM

Since its potential was discovered, AM-SLM has undergone rapid research and development [13]. Its capability to enable intricate metal structures makes it well-suited for constructing complex designs in RF and communication systems [35]. However, given its intended use for transmission, the unknown inherent noise in the component might limit its usability [22]. Consequently, analyzing the PIM within an AM-SLM component becomes relevant.

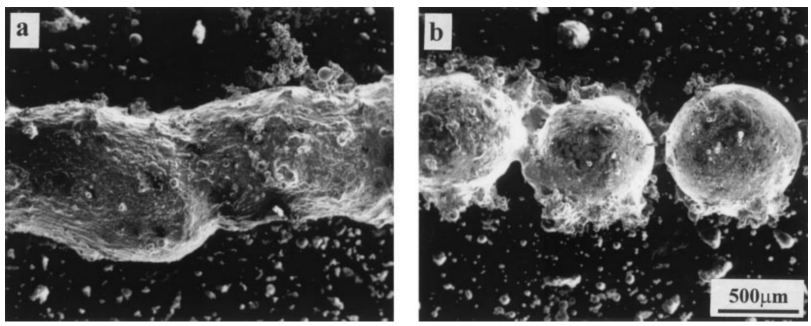

Figure 3.4: Reproduced Scanning Electron Microscope (SEM) images of laser sintered surfaces using different laser powers: **a**. 10 W, 1.0 mm/s. **b**. 100 W, 20 mm/s from [1] with permission.

There are a few factors within the AM-SLM process which might cause concern for PIM. As illustrated in Fig. 3.2, the component is made up of melted powder metal grains [46]. In the building process, several phenomena occur that modify the internal microstructure and surface of the metal, resulting in surface roughness and increased porosity within the metal print. This is demonstrated in the SEM images in Fig. 3.4, where partly melted grains can be seen. At the beginning of a scan track, more powder is available in the neighborhood of the printing area. These particles are attracted by the melt pool, creating a larger ball which cause roughness [49]. A related effect to that is called satellites. It occurs when some solid powder grains are directly connected with the melt pool. Since already having been formed into solid grains, these do not melt and are instead surrounded by liquid metal [49]. Another phenomena is called the balling effect, it occurs when the energy delivered to the melting pool is insufficient, resulting in a half-melted layer, see Fig. 3.4 [1]. Further, this is the main cause of porosity, hence the main concern in the printed components mechanical properties. These phenomena creating porosity and surface roughness can induce areas with concentrated surface currents, which as discussed in Section 2.3 would result in PIM detection.

3.3.1 Material Properties of AlSi10Mg

Aluminum is a preferable material for the aerospace and automotive sector since it is lightweight [50]. AM-SLM printing commonly use an aluminum age-hardenable cast alloy, AlSi10Mg, because of its good mechanical properties [46]. AlSi10Mg has been subjected to thorough research when it comes to process parameters, support structures, resulting microstructure, and mechanical properties [21, 51, 52]. In [21], 91 AM-SLM components were created from AlSi10Mg using varying platform temperature, building direction and peak hardening. All showed a reduced strength in the build direction and porosity was visible in all batches with pores generally below 300 μm. All samples exhibited a density above 99 % in relation to a test sample. Some material properties of AlSi10Mg compared to aluminum is presented in Table 3.2.

Table 3.2: Electrical and thermal characteristics of aluminum and AlSi10Mg materials.

Parameter	**Aluminum**	**AlSi10Mg**
Surface Roughness (H)	10.42μm	0.5μm
Surface Roughness (V)	4.43μm	
Electrical Conductivity	3.4×10^7 S/m	1.6×10^7 S/m
Relative Permeability	1.00021	1.00028
Thermal Conductivity	237.5 W/(mK)	170 W/(mK)
Thermal Expansion	2.33×10^{-5} 1/K	2.1×10^{-5} 1/K
Specific Heat	951 J/(kgK)	920 J/(kgK)

It is worth noting that the electrical conductivity is lower for AlSi10Mg than it is for aluminum. As discussed in Section 2.3, this is likely due to the higher porosity in AM-SLM materials. Further, as stated in Eq. (2.5), the lower electrical conductivity of AlSi10Mg indicates a higher skin effect. This in turn results in a higher impedance and a higher likelihood for PIM, as discussed in Section 2.3. In other words, a more porous material would be more likely to induce PIM.

3.4 Hot Isostatic Pressure Post Processing

HIP post-processing is a technique used in materials science and manufacturing to improve the properties of metal by densifying presintered components and consolidating powders. [53]. It entails subjecting a material to high temperature and pressure simultaneously within a gas-filled chamber [54]. Under these conditions, internal pores or defects within a solid body collapse and undergo diffusion bonding. Both encapsulated powder and sintered components are densified, resulting in improved mechanical properties and a reduction in the variability of properties.

Additive manufactured components possess a degree of porosity, as discussed in Section 3.3. Porous materials are more likely to crack, reducing their mechanical strength. The study in [55] demonstrates how employing HIP can effectively close these pores, a crucial step in attaining the desired characteristics of the printed

component. The characteristics have been studied for the mechanical properties, however the impact of HIP on the material in relation to PIM is yet to be explored.

Chapter 4

PIM Testing: Setup and Component Design

This chapter provides an overview of the test setup designed for PIM detection and the components that have been designed for this purpose. Section 4.1 offers an overview of the test setup, including the equipment used. Following this, Section 4.2 covers the fundamentals of RF theory relevant to component design. Following, Section 4.3 details the design of the Device Under Test (DUT) and factors considered in designing other components. Finally, Section 4.4 covers the methodology of the test being carried out.

4.1 Overview of Test Setup

The test setup is designed to measure PIM at the third order intermodulation (IM3) frequency. For accurate results, the setup is engineered to in itself induce low PIM levels and high filtering around the IM3 frequency. The measurements are taken at the IM3 frequency, since it is of the highest magnitude and therefore easiest to detect [56]. The setup is made for the X-band, hence frequencies between 8 GHz and 12 GHz. This allows for manageable dimensions in the mm-cm range when fabricating a printed test object.

The test setup is shown in Fig. 4.1. The setup begins with two signals being generated, f_1 at 7240 MHz and f_2 at 7625 MHz. This creates an intermodulation at 8010 MHz, as described in Chapter. 2. The frequencies are added in a Wilkison divider and then amplified in a Traveling Wave Tube (TWT) amplifier. From the decoupler the power level is measured and controlled. This is necessary since a higher power will generate stronger surface currents and thereby a higher PIM signals. By controlling the power, it is ensured that the same power is applied to the system when the PIM measurements are taken. The signal is then exposed to a chain of bandpass filters (BPF) to remove active IM3 products from the amplifier as well as PIM generated in the output waveguide from the amplifier. In between the filters there are high pressure flanges, designed to create a high pressure transition and thus lowering the PIM levels inherent in the connection between filters as described in Section 2.2. The Device Under Test (DUT) is engineered to resemble a rectangular coaxial waveguide, made to be likely to generate PIM from high surface currents. The power is radiated out through a horn and into an isolated PIM chamber. Another horn capture some of the radiated effect, filters it first through a BPF and then through a highpass filter (HPF) to focus on the 8010

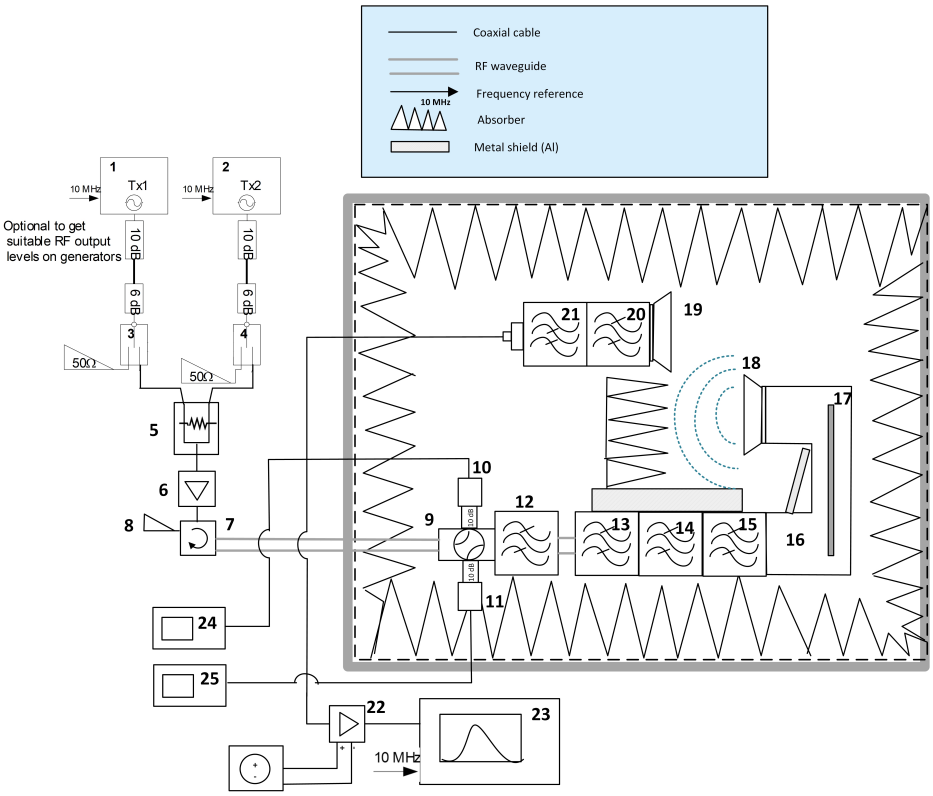

Figure 4.1: Test setup for PIM measurements including PIM chamber. Numbered components can be found in Table 4.1.

MHz frequency. Lastly, the signal is amplified and measured through a spectrum analyser. The gray areas indicate the non-RF equipment. The dark striped areas indicate where there is a high pressure interface. A full list of the test equipment used can be found in Table 4.1.

As mentioned in Section 2.2, all metal contacts contribute with PIM. Therefore, the anechoic chamber plays an important role in improving the accuracy of PIM measurement and is used to block out contributions from metal sources in the surroundings. Most anechoic chambers employ pyramid absorbers made to lower the background PIM from the test setup itself [8].

Table 4.1: Equipment for test setup

Pos.	Instrument Type
1	Signal source, Tx1 at 7625 GHz
2	Signal source, Tx2 at 7240 GHz
3	RF Door Safety Switch
4	RF Door Safety Switch
5	Wilkison divider to mix the signal and create IM products
6	TWT amplifier
7	Circulator, to avoid reflection of signal
8	High power load
9	Waveguide directional decoupler, setup to continuously monitor the power level
10	RX chain monitor power sensor
11	RX chain monitor power sensor
12	Out of band noise filtering for the TX signal (BP)
13	Out of band noise filtering for the TX signal (BP)
14	Out of band noise filtering for the TX signal (BP)
15	Out of band noise filtering for the TX signal (BP)
16	Device under test (DUT)
17	Changeable metal sample inside DUT
18	TX horn to radiate PIM frequency at 8010 MHz
19	RX horn to collect PIM
20	RX filter (BP), suppress coupled TX power in order to avoid IM in the LNA
21	Highpass transformer(HP), adds additional filtering
22	LNA, amplify the PIM signal, powered by voltage supply
23	Spectrum Analyser
24	Power meter RX chain
25	Power meter TX chain

4.1.1 Link Budget

As discussed in Section 2.2, PIM occur at low signal levels and the test setup has been engineered with a suitable link budget. To evaluate what a suitable link budget might be, a communication link between a standard phone to a satellite has been calculated. The example is shown below, where the received power is expressed as

$$P_{RX} = P_{TX} + G_{TX} - L_{path} + G_{RX} \tag{4.1}$$

where P_{RX} and P_{TX} is the power at the receiving and transmitting antenna. G_{RX} and G_{TX} is the gain of the antennas. L_{path} is the path loss. Further, L_{path} is

defined by Friis' free-space path loss equation

$$L_{path} = 20\log_{10}(d) + 20\log_{10}(f) + 20\log_{10}(4\pi/c) \tag{4.2}$$

where d is the distance between the antennas and f is the frequency. Using a standard satellite distance of 36 000 km and setting the frequency to the desired signal frequencies 7240 MHz and 7625 MHz, the path loss can be calculated to 210 dBm. An average gain value for a horn antenna is 10 dBi, where dBi stands for "decibels relative to an isotropic antenna." It is a unit of measurement used to express the gain of an antenna. An average power for a transmitting terminal is 10 W and power in watt can be translated to dBm using the following

$$P_{\mathrm{dBm}} = 10 \times \log_{10}\left(\frac{P_{\mathrm{W}}}{0.001}\right) \tag{4.3}$$

meaning 10 W equals 40 dBm. Using these values, the received power can be calculated as: 40 dBm + 10 dBi − 201 dBm + 10 dBi = −161 dBm, equal to 7.95×10^{-17} W. This is a very low received power, compared to the 10 W transmission power. Based on this, the setup is engineered to reach approximately around −161 dBm on the RX side to read the PIM signal.

Angle Misalignment Loss

In the link budget described in Section 4.1.1, the antenna gain is initially set to an average value. However, for a more precise calculation of the antenna gain, it is necessary to consider factors such as the aperture, angle, and distance between the antenna horns. When performing an accurate calculation of the antenna gain, the radiation patterns of the horns should be taken into account.

A simplified model for calculating the antenna gain is presented below. The peak gain of the antenna in linear terms is calculated as

$$G_0 = \eta_0 \times \eta_L \times \frac{4\pi A}{\lambda^2} \tag{4.4}$$

where λ is the wavelength in free space, A is the aperture area and η_0 is 0.81 for a rectangular horn. η_L is a value between zero and one and is approximated by the losses. G_0 is then converted to dBi, to express the gain of the antenna as

$$G_{0_{\mathrm{dBi}}} = 10\log_{10}(G_0) \tag{4.5}$$

When considering the loss of the antennas, the gain reduction due to angular misalignment needs to be factored in. Calculating the loss is done as

$$L_{\mathrm{misalignment}}(\mathrm{dB}) = 12 \times (\frac{\theta}{\theta_{3dB}})^2 \tag{4.6}$$

where θ is the angle of misalignment between the antennas and $\theta_{3\mathrm{dB}}$ is the half-power of the antennas. The half power beamwidth refers to the angular width of the main lobe of an antenna radiation pattern has decreased to -3 dB. It is calculated as

$$\theta_{3\text{dB}} = \frac{k \times \lambda_0}{\text{L}} \tag{4.7}$$

where k is a constant derived from empirical measurements on horn antennas and equals 70 for the H-plane and 50 for the E-plane. L represents the dimension of the horn in either the H-plane or the E-plane, depending on which plane the calculation is being performed for. The final expression for the antenna gain is expressed as

$$G_{\text{dBi}} = G_{0_{\text{dBi}}} - L_{\text{misalignment}} \tag{4.8}$$

Following the simplified model in (4.4) to (4.8), the antenna gain can be calculated while accounting for the angle alignment loss. This model is based on a Gaussian distribution and should be used with caution for angles greater than 15°. In applications like satellite communication and point-to-point microwave links, angle misalignment of horn antennas can significantly degrade signal quality, making it a crucial consideration in the setup. In satellite communication, uplink transmitters typically operate at 1 to 10 watts (30 to 40 dBm), while downlink receivers handle much lower power levels due to the distance from the satellite.

4.2 RF Component Theory and Design Strategies

The performance of the PIM tester is significantly influenced by the PIM level of the electronic components within the setup, as discussed in [8]. Consequently, the design of the components used in the test setup has been carefully carried out, taking into account factors such as their individual PIM levels, contact pressure, and propagating modes. All components have been simulated and designed in HFSS before manufacture.

4.2.1 Waveguides

At frequencies above 1 GHz, conventional cables and coaxial lines experience significantly higher losses. Consequently, when dealing with power levels in the megawatt range or 60 dBm, transmission through cables becomes impossible [24]. To minimize dielectric and radiation losses, as well as reflections, waveguides can be used above 1 GHz frequencies. Waveguides are made to guide electromagnetic waves through high frequency appliances where the wavelength approaches the cross-sectional dimensions of the rectangular waveguide (WR). The dimensions of a waveguide are directly related to the frequency of the signals passing through it. For instance, at a frequency around 7 GHz, the waveguide opening would be approximately 2 cm. However, at a lower frequency like 1 GHz, the opening would need to be over 16 cm. It is essential to consider the practical limitations of waveguide dimensions when designing for specific frequencies. The higher the frequency, the more common it is with waveguides. Within the space industry, it is common practice to use cables up to 2-4 GHz.

The theory behind WR are based on Maxwell's Equations, resulting in the formation of guided modes along the waveguide structure. Mode propagation is a

key concept, since different WR geometries support different modes of propagation. Maxwell's equations are formulated as

$$\nabla \cdot \mathbf{D} = \rho \tag{4.9}$$

$$\nabla \cdot \mathbf{B} = 0 \tag{4.10}$$

$$\nabla \times \mathbf{E} = -\frac{\partial \mathbf{B}}{\partial t} \tag{4.11}$$

$$\nabla \times \mathbf{H} = \mathbf{J} + \frac{\partial \mathbf{D}}{\partial t} \tag{4.12}$$

where $\mathbf{D}$ is electric flux density, ρ is charge density, $\mathbf{H}$ is magnetic flux density, and $\mathbf{J}$ is conduction current density. The wave equation in one dimension can be derived from Maxwell's equations, particularly the wave equation for electromagnetic waves for source free regions

$$\frac{\partial^2 u}{\partial t^2} = v^2 \frac{\partial^2 u}{\partial x^2} \tag{4.13}$$

where $u(x,t)$ is the displacement of the wave, t is time, x is position, and v is the wave velocity.

In vacuum, the wave equation for an electromagnetic field $E(x,t)$ is given by

$$\nabla^2 \mathbf{E} - \frac{1}{c^2} \frac{\partial^2 \mathbf{E}}{\partial t^2} = 0 \tag{4.14}$$

where ∇^2 is the Laplacian operator, c is the speed of light, and t and x represent time and position, respectively.

For one-dimensional waves, this equation simplifies to

$$\frac{\partial^2 E}{\partial x^2} - \frac{1}{c^2} \frac{\partial^2 E}{\partial t^2} = 0 \tag{4.15}$$

Comparing this equation with the general form of the wave equation in Eq. (4.13), it is clear that $u(x,t) = E(x,t)$ and $v = c$. The wave equation expresses how these waves propagate through a medium.

In waveguide theory, modes refer to specific patterns of the electromagnetic field distribution that can propagate within the waveguide structure [24]. Each mode corresponds to a particular set of electromagnetic field patterns and propagation characteristics, which are determined by the frequency and geometry of the waveguide. The most common types of modes in waveguides are the transverse electric (TE) mode and the transverse magnetic (TM) mode, as depicted in Fig. 4.2 [57]. In the TE mode, the E-field is fully perpendicular to the direction of propagation (z-axis), while in the TM mode, the H-field is fully perpendicular to the z-axis. The transverse electromagnetic (TEM) mode, which has both the E and H fields perpendicular to the z-axis, is not achievable in waveguides because it would imply either the contribution of E_z or H_z equals zero [24]. This contradicts the fundamental nature of waveguides, which requires some form of boundary conditions to guide electromagnetic waves along a path. However, this mode is possible in coaxial cables or open space where confinement is not an issue. This is because the structure of coaxial cables inherently allows for both the electric and

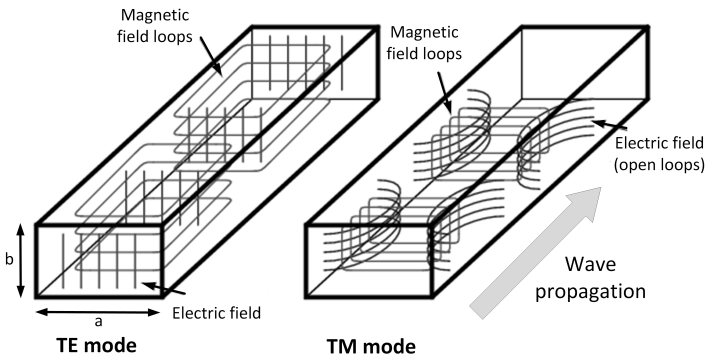

Figure 4.2: Electric and magnetic fields in the TE and TM modes.

magnetic fields to be perpendicular to the axis, making the TEM mode achievable in such configurations.

Another important property of waveguides is the cutoff frequency, which indicates the frequency below which the waveguide does not support the propagation of a particular mode [24]. For rectangular waveguides, which are extensively used in this research, the cutoff frequency is expressed by the equation

$$f_{c(m,n)} = \frac{c}{2}\sqrt{\left(\frac{m}{a}\right)^2 + \left(\frac{n}{b}\right)^2} \tag{4.16}$$

where, c is the speed of light, (m, n) represents the mode indices, and a and b denote the width and height, respectively, of the waveguide opening. The mode indices (m, n) determine the number of half-wavelength variations along the two orthogonal directions of the waveguide cross-section. Similarly, the wavelength in free space at the cut-off frequency, as a function of mode indices and waveguide dimensions, can be calculated as shown in Eq. (4.17). The wavelength in free space is simply $\lambda_c = \frac{c}{f_c}$.

$$\lambda_{c(m,n)} = \frac{2ab}{\sqrt{m^2b^2 + n^2a^2}} \tag{4.17}$$

Waveguides are one of the base components of this research and waveguide theory apply to all components designed and used in the test setup. The TX chain is built by WR112 interfaces with cavity dimensions of $a = 28.4988$ mm, $b = 12.6238$ mm, to adjust to frequencies between 7.05 to 10 GHz. Conversely, on the RX chain is built by WR90 interfaces with cavity dimensions of $a = 22.86$ mm, $b = 10.16$ mm, to adjust to frequencies between 8.20 to 12.40 GHz.

4.3 Design of DUT for PIM Generation

Recent studies have shown that PIM is a current related nonlinearity [26], [58]. Therefore the test object is engineered to induce high surface currents, to generate

PIM of measurable levels [26], [58]. As described in Section 3.3, the partly melted powder grains cause porosity, unevenness and cracks, which would result in areas of high surface currents. To measure the effect of these surface currents, a rectangular coaxial waveguide is designed, see Fig. 4.3a. The cavity inside the component is shown in 4.3b. It is important to understand that HFSS models cavities in a perfectly conducting medium, therefore what is shown in the picture is the cavity within the component shown in 4.3a. It is made to match a WR112 interface on the TX side and then transition over to a WR90 interface on the RX side, hence the quarter-wavelength transition on the RX end. Fig. 4.3c and Fig. 4.3d illustrate the transition of the propagating TE_{10} at the waveguide opening to the TEM mode in the channel, inducing strong fields around the center conductor.

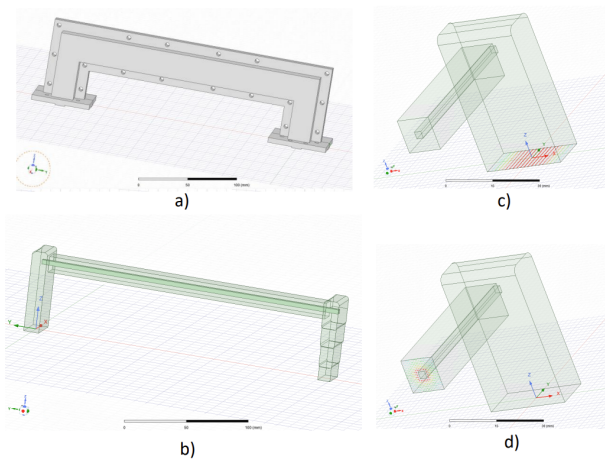

Figure 4.3: Illustrations of the DUT in HFSS. The models shown are the cavities in a perfect conductor. **a**. CAD overview of the component. **b**. The cavity inside showcasing the center conductor. **c**. Indicated TE_{10} field at the waveguide opening. **d**. Strong TEM fields exhibited around center conductor after transition.

Previous research conclude that distributed PIM on a transmission line is produced along the length of the line [9]. Hence, it is deemed advantageous for the test object to have considerable length to generate PIM. With the AM-SLM build plate constrained to 25 cm x 25 cm, the center conductor has a length of 25 cm. The center conductor's thickness is determined by several factors. First, to accommodate surface currents which as discussed in Section 2.3 reach into the material a few micrometers by the skin effect in Eq. (2.5). Secondly, the thickness also has to be designed to ensure that the waveguide tunnel width remains below half a free space wavelength to avoid the creation of unwanted waveguide modes. Given that the impedance of the coaxial waveguide is defined by the ratio of R_1 to R_2, adjustments in the tunnel width directly impact the center conductor width. Lastly, these dimensions are calculated to withstand the AM-SLM process without breaking, bending, or deforming.

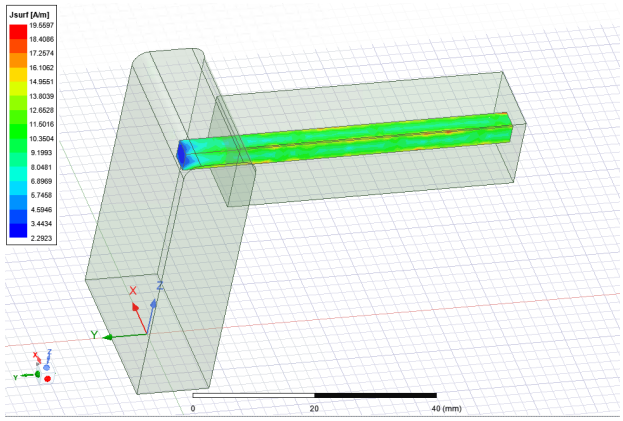

Figure 4.4: Generated surface current in DUT along the center conductor in HFSS.

The center conductor has a rectangular cross-section. Partly because this replicate the majority of real life applications, such as rectangular waveguides and standard block components, though it is also because sharp edges tend to induce higher surface currents, as shown in Fig. 4.5. The design of the setup aims to simulate a worst-case scenario, hence the intentional generation of high currents is desirable.

4.3.1 Design of High Pressure Flanges

As discussed in Section 2.2, all points of metal contacts are be prone to generate PIM. However, by applying additional mating force between these surfaces, the metal points of contact can be pressed together to increase the contact surface area and reduce current saturation within the connection [14]. Therefore, high pressure flanges have been designed to interface between the components. The pressure applied is determined by the ratio of force to area, described as

$$P = \frac{F}{A} \tag{4.18}$$

where A is the total area of the heightened pressure platforms. The force applied stems from the fastener screw torque clamp force. It is calculated from the torque, diameter and coefficient of turning friction, as described in Eq. (4.19).

$$F = \frac{T}{c_f D} \tag{4.19}$$

where T is torque required, D is the nominal bolt diameter and c_f is the coefficient of friction constant. For aluminum c_f is between 0.2 and 0.5 [59].

The flanges are designed to reach as high pressure as possible. The components are made out of aluminum which reach elastic deformation at 70 MPa [60], hence pressure approaching that limit is the highest pressure possible before deformation. Each screw of type M4 is calculated to deliver a 2500 N clamping force and the area

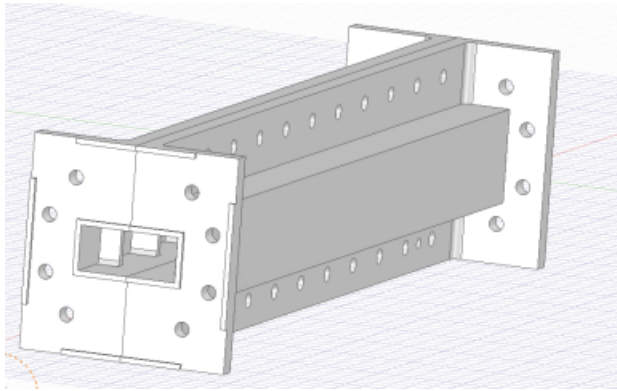

Figure 4.5: Designed high pressure flange for TX bandpass filter.

is calculated accordingly. The full seal around the cavity provide a high pressure between the interfaces, and the surrounding elevated surfaces in the outermost circle acts as support platforms to spread the pressure and prevent deformation.

The high-pressure interfaces are primarily designed for the TX components, aiming to suppress PIM effectively in the TX chain. Each component features a high-pressure flange that connects to a flat surface. Two BPFs, each with four screw holes, were available in-house. Due to the filters being limited to four screws, the pressure can only reach 50 MPa, instead of the 70 MPa.

Increasing the number of filters in the setup will remove more PIM. Nonetheless, the connections between the filters introduce additional PIM into the system. While high-pressure flanges can mitigate induced levels, achieving the ideal high pressure of 70 MPa may not be feasible. Nevertheless, the combined impact of multiple filters ensures that induced PIM levels remain low, even with the pressure around 50 MPa.

A full view of the high pressure flanges can be found in Appendix A, Fig. A.8.

4.3.2 Design of Filters

As illustrated in Fig. 4.1, multiple TX filters are installed in series to isolate the signal and reduce noise. Since PIM events occur at very low signal levels, as shown in Section 2.2, filtering play a critical role in attenuating noise and interference from other frequencies. The in-house filters each contributed with an isolation of approximately 35 dB, collectively reducing the system noise by 70 dB. To further enhance noise reduction, two more BPFs were designed using HFSS software. Initially, the existing TX filters were measured and modeled to ensure the same frequency band was filtered to pass through. Thereafter, additional cavities were integrated into the HFSS design to achieve a steeper roll-off, resulting in an isolation of 65 dB per filter. The total isolation is then approximately 200 dB, which is sufficient for PIM measurements.

The milling manufacturing process presents another important consideration. Unlike AM-SLM, milling is reliant on a drilling tool cutting out material. Due to the fragility of the milling tool tip and that it in itself consists of a radius, fillets

must be incorporated into hardware components to prevent damage and ensure proper operation. It is recommended to use a fillet radius of one-tenth of the depth to accommodate the milling tool effectively.

However, in RF technology, precise cavity and structure dimensions in the range of 0.01-0.05 mm are crucial. Adding a fillet without proper alterations can impact these dimensions significantly. When modifying a cavity, Eq. (4.20) is employed to maintain consistent electromagnetic properties.

$$a = a_0 + \frac{1.717}{2}\frac{r^2}{b} \tag{4.20}$$

where a is the new width, a_0 is the original width, b is the height of the cavity and r is the radius of the fillet.

4.4 PIM Measurement Methodology

Due to the complexity and uncertainty of PIM sources, measurement is the most important means to study and evaluate the PIM performance of wireless communication system [8]. This section will present the method used when conducting the PIM measurements. The section includes a preparation checklist, handling of the equipment and how the tests were executed.

4.4.1 Handling of RF Equipment and Safety Precautions

The hardware is to be handled with lint free gloves to protect the RF components and avoid contaminants from outside environment to induce PIM products. Extra caution ought to be taken in regard to the high output powers of the TWTs, as the radiated effect can cause burns and vision impairment. This is done by a master switch, preventing the TWT to operate unless the anechoic chamber is sealed. Before the test campaign all instruments are checked for calibration, and functionality.

4.4.2 Test Execution

Before any test, the test equipment is given a sufficient warm up time. This is around 30 minutes and ensures the functionality of the inherent calibration in the equipment. See Table 4.2 for a written checklist to follow before and during the test campaign.

Once the checklist has been covered, the power meters were calibrated to measure the power at the point right before the DUT object, to know the power applied to the DUT. The power meters were re-calibrated every 24 hours to ensure the calibration was up to date.

The sample was then inserted into the DUT object. Measurements were taken at different power levels, spanning from 40 dBm to 50 dBm. This corresponds to 10 W to 100 W applied to the DUT object. Each set of testing started with a measurement of the reference sample, then the printed samples, and finally the reference sample again to check and take into account any variations in the setup such as temperature changes or shifting of isolating materials.

Table 4.2: Preparation Checklist

Item
Visually inspect the Rohacell chamber
Control no blockage of the TWT air filter
TWT has been tested at correct frequency and outputted sufficient power
Spectrum analyzer has been tested
Signal generator has been tested
Function of LNA has been controlled
Microwave switches is connected to safety switch
Instruments, components, and cables are at the test site
Calibrate instruments and components listed in Table 4.1 have been checked

Chapter 5

Characterization of PIM in AM-SLM RF Components

This chapter holds the results from the PIM measurements on milled and AM-SLM printed RF components. Section 5.1 displays a visual comparison between the AM-SLM printed and milled sample. Section 5.2 gives an overview of the realizes test setup, covering the S-parameter measurements of the chains and a calculation of the horn antenna gain. Section 5.3 provides the experimental results, comparing the PIM performance of AM-SLM printed samples to that of milled reference samples. Finally, Section 5.4 discusses the results of the PIM characterization.

5.1 Visual Comparison of Samples

When visually inspecting the samples, the printed ones are distinguishable from the milled sample. The samples are depicted in Fig. 5.1. At the bottom is the milled sample, in the middle is an AM-SLM printed sample shown from the vertical printing direction and at the top is an AM-SLM printed shown from the horizontal printing direction. Based on the reflections in the metal surface, the sticks increase in surface roughness. This is in line with the parameters presented in Table 3.2, where the surface roughness for the vertical print is 8.8 times higher than that of a milled sample, and the horizontal print is over 20 times higher.

To investigate the printed samples further, SEM pictures were taken. The pictures are presented in Fig. 5.2, where the surface has been captured at a resolution of 2 mm and at 300 μm. In both, the surface roughness is visible. In addition, at 300 μm, the balling effect discussed in Section 3.3 can be seen. The partly melted grains create sub-micron nodules along the printed structure. These features are absent in the milled aluminum samples.

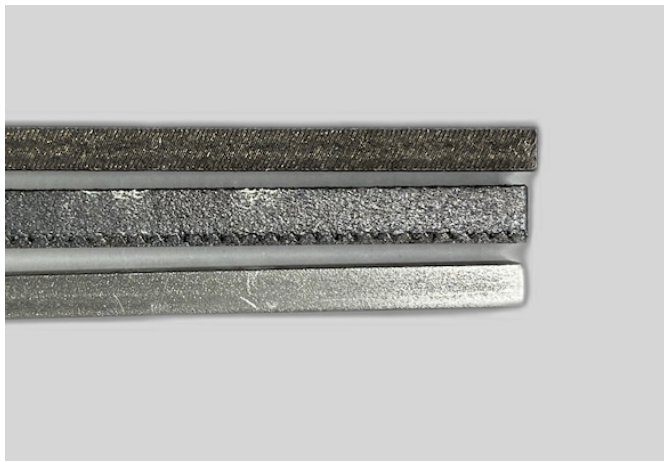

Figure 5.1: Metal samples for PIM test, from bottom: milled aluminum, AM-SLM vertical print, AM-SLM horizontal print.

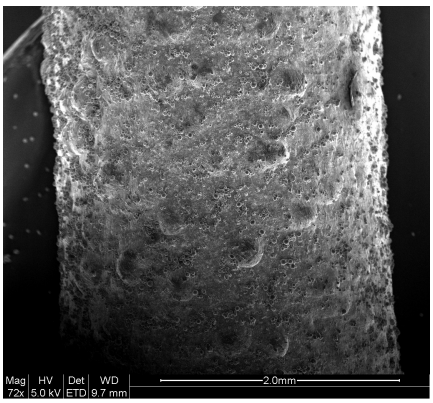

(a) AM-SLM printed samples at 2.0 mm.

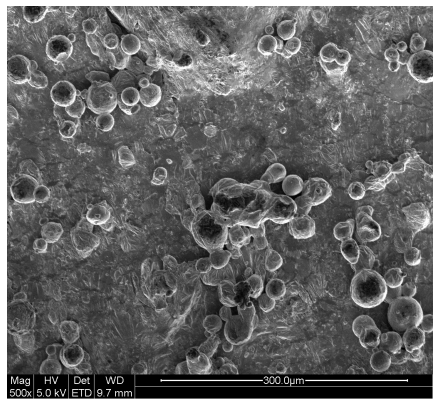

(b) AM-SLM printed samples at 300 μm.

Figure 5.2: SEM images of AM-SLM printed samples showing the surface roughness and the balling effect.

5.2 PIM Test Setup Realization

In the test setup, three frequencies are of importance. The first two frequencies, 7240 MHz and 7625 MHz, carry the generated signals, while the third frequency, 8010 MHz, is the IM3 frequency responsible for carrying the intermodulation product. For the setup to function effectively, it is essential that these frequencies exhibit a low S_{11} value.

A low S_{11} value indicates that a minimal amount of signal is being reflected back from the device to the component, meaning there is a minimal signal loss and the power transfer efficiency is maximized. This is important in PIM measurement setups, since the received power levels can be as low as 10^{-19} W.

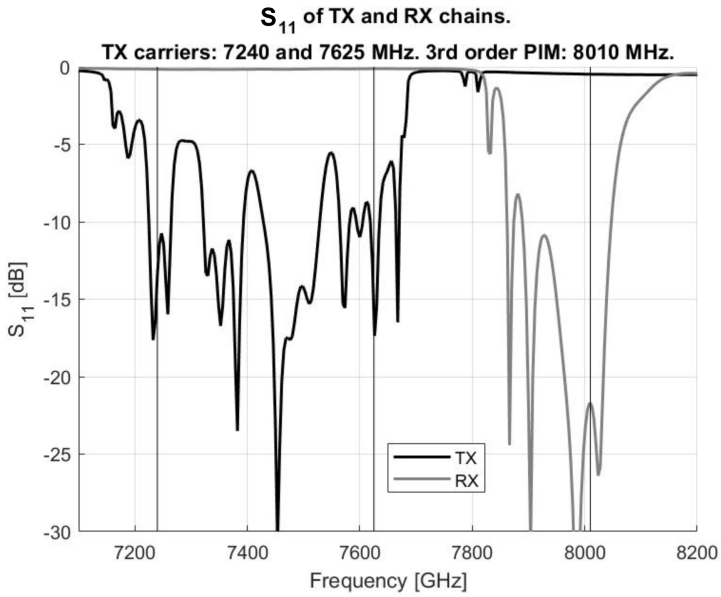

Figure 5.3: The S_{11} component of the TX and RX Chain with markers added at 7240 MHz, 7625 MHz, and 8010 MHz.

To assess the S_{11} parameter, both the TX and RX chains were measured using a Vector Network Analyzer (VNA). The results, depicted in Fig. 5.3, reveal a drop in the S_{11} parameter for the TX chain at the designated frequencies of 7240 MHz and 7625 MHz. Similarly, on the receiving end, the S_{11} parameter drops for the IM3 frequency at 8010 MHz. This observation serves to underscore that the setup and the designed components are functioning as intended.

Fig. 5.4 shows the TX and RX chains mounted in the anechoic chamber. Since PIM can originate from any metallic contact, extra isolation material is used to shield the horns from PIM reflections caused by the metallic filter structures. Additionally, flat metal pieces are positioned to reflect RF waves away from the horn aperture, ensuring that only the radiated effect from the TX horn is captured. All additional metal pieces are isolated from each other using plastic at the contact surfaces.

During testing, the DUT is demounted to change the sample inside. The DUT is then remounted in the same position.

The signal is generated, mixed, and amplified in the TWT. After passing through four filters, it reaches the DUT. Once it passes over the test sample, it is radiated through a horn and captured by another horn. During this transmission, some of the signal is lost. Knowing the magnitude of this loss is crucial because the signal is measured at the RX horn. To obtain the actual value, the calculated loss must be added to the measured PIM level as

$$P_{\mathrm{RX}_{\mathrm{measured}}} = P_{\mathrm{TX}_{\mathrm{real}}} + L_{\mathrm{losses}} \tag{5.1}$$

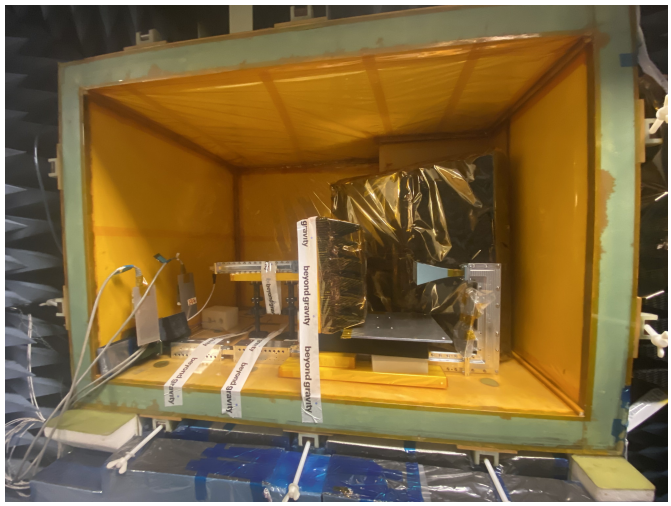

Figure 5.4: Overview of the realized test setup in the anechoic chamber, showing isolating material, the TX and RX chain.

The loss is calculated as described in Section 4.1.1. The aperture dimensions of the TX and RX horn is measured to 74 mm $\times$ 55 mm and 119 mm $\times$ 40 mm respectively. The misalignment angle between the horns center points is measured to 45°and the horns are radiating in the H-plane direction, corresponding to toward in Fig. 5.4. Using equation (4.4) to (4.8) the loss due to misalignment is calculated. The value of η_L is estimated to 0.98.

The calculations from the simple model presented in Section 4.1.1 are shown in Fig. 5.5, where the loss is displayed over varying angles. This simple model is based on a Gaussian distribution. To verify these results, a more complex method presented by Balanis in [2] was also implemented. This model was used to double-check the loss due to the wide angle of 45° between the horns.

As seen in Fig. 5.5, the simple model deviates from the Balanis model, particularly on the RX side. The gain for both the RX and TX horns is 17.7 dBi each. It is a coincidence that the gains are almost identical. Additionally, 1 dB is subtracted to account for losses and phase errors that reduce the gain.

Using Eq. 4.2, the free space path loss is calculated to be 74 dB. Compared to the expected average value of 10 dBi for a horn antenna presented in Section 4.1.1, it is large. This will alter the level of the PIM measurements presented, as the measurements were taken at levels around or below -100 dBm but will be showcased at a level of -30 dBm. However, in practice, this is less critical as measurements are taken for comparative purposes, emphasizing the significance of relative levels rather than absolute values.

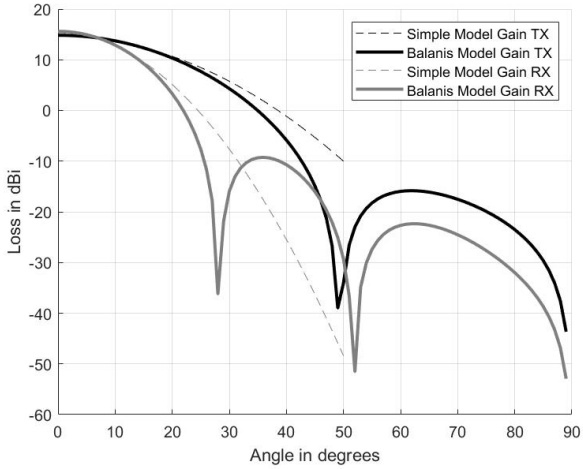

Figure 5.5: The loss of the TX and RX horns showed over a range of misalignment angles for both a simple model and the Balanis model [2]. At 0° the horns are directly facing each other and as the horns are directed from each other, the angle increase.

5.3 Experimental Results

Following are the results from the research study. Each AM-SLM sample was measured three times during testing, with each set beginning and ending with the reference sample. This approach was used to monitor changes in PIM levels over time.

5.3.1 Comparison of AM-SLM and Milled PIM Performance

Fig. 5.6 present the PIM level of the milled rectangular sample, as well as the AM-SLM printed rectangular samples. All three sample pins are showed individually, to show that all exhibited a higher PIM level than the milled reference. The printed samples are on average 5 dBm higher than the references. Worth mentioning is that at the end of each set of measurements, the reference PIM showed a different PIM level than it did in the first measurement. This is common in PIM test setups and will be discussed more later. One can also notice that the PIM level is at a high level starting at -50 dBm, and not the low level of -150 dBm as calculated. This is because of the misalignment loss between the antennas and it will be discussed further in Section 5.4.3.

From Fig. 5.1, it is evident that the printed samples exhibit higher porosity and surface roughness, as indicated by the duller reflection. This observation aligns with the predicted surface roughness values presented in Table 3.2. Further, Table 3.2, states that the electrical conductivity is higher in milled material than in printed. As argued in Section 2.3, the electrical conductivity and surface roughness is tied to PIM. As proven in Fig. 5.6, the printed samples do have a higher PIM

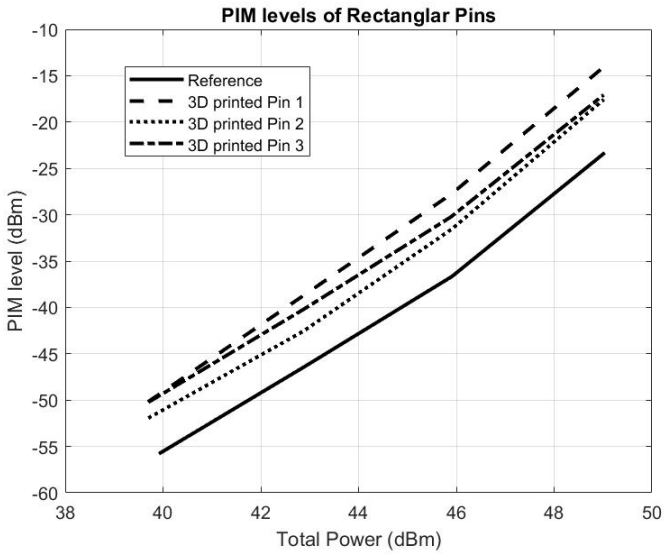

Figure 5.6: PIM levels of milled reference pin and AM-SLM 3D-printed pins. A lower level indicate a better performance.

level, providing evidence supporting the proposed relationship between porosity in AM-SLM materials and PIM.

5.3.2 Comparison of Circular and Rectangular Samples

At the edges and corners of a conductor, charges tend to accumulate because these regions have higher curvature. This leads to a higher electric field intensity near the edges. The test samples are chosen to be rectangular, as discussed in Section 4.3, to replicate real-world applications and because they induce higher PIM levels. However, by studying samples with a circular cross-section it is possible to relate the surface area to the amount of induced PIM.

For this purpose, one circular pin was printed using AM-SLM, and another was milled. The results are presented in Fig. 5.7. As observed, the milled samples exhibit better PIM performance compared to the AM-SLM printed samples. Additionally, the circular pins have a lower PIM level overall, as hypothesized, due to the absence of the sharp edges present in rectangular samples. It is worth noting that the data for circular pins come from a single sample and one measurement due to an instrument failure.

5.4 Discussion Regarding PIM Results

So far in this chapter, the final realization and functionality of the PIM setup were presented, alongside the results of measured PIM values on milled and AM-SLM printed aluminum samples. Following this, tried methods to mitigate PIM will be

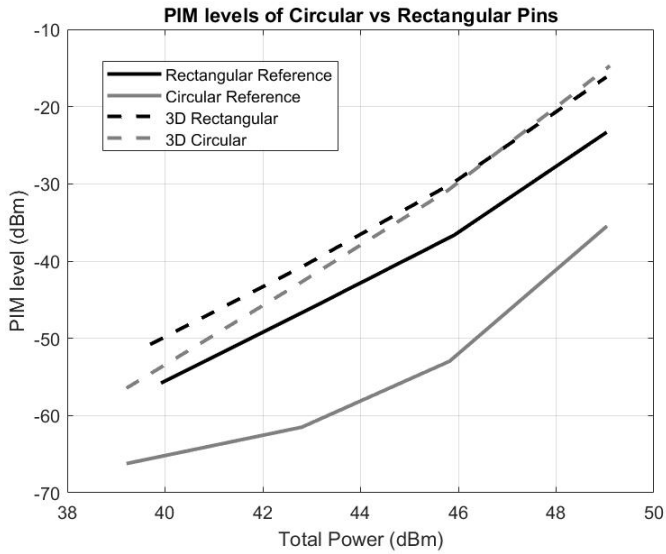

Figure 5.7: PIM level results of circular and rectangular samples, both milled and AM-SLM printed.

outlined. Additionally, observations regarding deviations will be discussed, and an examination of the impact of antenna gain will be provided.

5.4.1 Methods to Mitigate Surrounding PIM

First, the isolation of the setup will be discussed. When setting up the instrument and equipment in the PIM chamber, the importance of isolating materials quickly became evident. Before any tests were performed, the PIM of the test chamber was effectively lowered by adjusting the placement of isolating material. This adjustment allowed the actual PIM signal from the sample to be measured without interference from other PIM sources within the setup. Additionally, the tightness of the screws proved to be crucial. As discussed in Section 4.3.1, high-pressure interfaces are important to mitigate PIM. This became clear during measurements, as tightening the screws between the filters and the horns noticeably reduced PIM levels. Therefore, implementing high-pressure flanges proved to effectively reduce PIM.

5.4.2 Deviation in PIM Measurements

Next, the reference measurements will be discussed. At the beginning and end of each test set, the milled reference sample underwent testing. This evaluation aimed to ascertain whether the PIM level measured on the same sample varied from the start to the end of the test. PIM is known to alter slightly from one measurement to another, with deviations in the PIM measurement setup expected to range from ± 1 dB to ± 3 dB.

The measurements on the reference sample between the first and last tests showed an average deviation of ±5 dB. The reason for the slightly increased deviation is difficult to pinpoint. Speculations include the tightness of the screws as the DUT is mounted and dismounted during sample changes. Another possibility is that as the test runs, the TWT warms up, potentially impacting the amount of active intermodulation it emits into the system.

Additionally, the opening and closing of the door to the PIM chamber between tests could contribute, as a less tight seal might allow more external PIM to seep through. However, it is important to note that all these factors should affect all samples equally. Therefore, the slight increase in deviation is deemed acceptable.

5.4.3 Impact of Antenna Gain

Another noteworthy aspect is the gain of the horn antennas. The graph depicted in Fig. 5.5 was derived after the tests had been conducted. During the tests, the misalignment gain was initially estimated to be around 20 dBi. However, subsequent calculations in Section 5.2 revealed a significantly worse loss, estimated at 74 dBi. As depicted in Fig. 5.5, the loss increases as the angle between the horns increases. While this trend was expected, the severity of the loss was underestimated.

A reduction in loss would have been achieved by directing the horns towards each other at a smaller angle. Consequently, this would have led to a higher measured PIM level for the same input power. However, this rise in PIM level would impact not only the tested samples but all intermodulation components within the setup, both passive and active. Consequently, there exists the possibility that the recorded PIM in the reference samples may include contributions from active intermodulation induced by the TWT or PIM from the surrounding environment.

It is plausible that the actual PIM from the milled sample may be drowned by internally generated PIM within the setup. With this reasoning, the observed additional 5 dB in the AM-SLM measurements may be attributed to chance, as these measurements by luck surpassed the setup's internal PIM level by 5 dB. Although seemingly unlikely, it is a factor to consider when interpreting the reliability of the results.

It is also important to consider that both the Balanis and the simple model used to analyse the gain are based on rough approximations. For example, the aperture on the RX horn is long and narrow, which would deviate from both models. An S-parameter measurement would have to be taken to know the actual value. However, since the circular stick does reach a lower PIM level as anticipated, it is reasonable to assume that the PIM contribution within the setup is sufficiently low to allow for accurate measurement of PIM from the samples.

5.4.4 Alternative Non-radiating Setup

The current setup has an issue due to the radiation path through the horns. This radiation can introduce PIM from external sources as the signal is transmitted between the two horns. An alternative approach involves constructing a closed setup where the TX and RX chains are isolated from each other. This isolation can be achieved using a diplexer.

A diplexer is a device that combines or splits signals based on their frequency. It operates by allowing signals of different frequencies to pass through separate channels, thereby isolating them from each other. By implementing a diplexer in the setup, the TX and RX paths can be effectively separated, minimizing the potential for external PIM interference. This ensures that the only PIM measured originates from the object under test, as the closed system prevents external signals from contaminating the measurements.

By implementing this setup, the use of horns becomes unnecessary. The isolation provided by the diplexer allows for a more controlled environment, increasing the accuracy of the PIM measurements. This alternative approach will ensure that the measured PIM levels are only coming from the test object, which improves the reliability and precision of the results. Thereby, this setup is an improvement over the current method, addressing the issues related to external radiation and providing a more reliable framework for PIM testing.

Another approach would involve developing the test object itself. The test object could instead be designed as an interdigital filter or a coaxial resonator filter, both of which are advanced types of electronic filters used to select or reject specific frequency ranges.

An interdigital filter consists of a series of parallel conductive fingers that create a resonant circuit through capacitive and inductive coupling. A coaxial resonator filter uses a coaxial cavity to achieve resonance. Both are structures where the current passes through the structure. As the current pass, resonances would occur, which would increase the current densities at specific points. By printing these filters using AM-SLM techniques, the current must pass through the material itself, allowing for a direct evaluation of the material's performance under high-current conditions.

This approach takes advantage of the inherent capabilities of AM-SLM in producing complex geometries and directly integrates the material into the operational environment of the filter. Further, designing the test object as a functional filter aligns the testing process more closely with practical applications.

5.4.5 Evalution of AM-SLM in Real-world Applications

AM-SLM allows for the fabrication of complex and intricate geometries that are difficult or impossible to achieve with traditional manufacturing methods. This is particularly useful for electromagnetic structures that require precise and unconventional shapes, such as waveguides, antennas, and filters.

The results in Fig. 5.6 indicate that the PIM level of AM-SLM components is, on average, 5 dBm higher than that of milled materials. Despite this increase, the difference is sufficiently small to render AM-SLM a viable manufacturing method within both the space and mobile industries. This minor increase in PIM levels is generally acceptable within these sectors, given the numerous benefits that AM-SLM offers, including design flexibility, reduced material waste, and the potential for integrating multiple functions into a single component.

While further research is necessary to fully understand the relationship between PIM and AM-SLM, the initial findings are promising. It is important to note that these results are based on pure, unprocessed AM-SLM samples. Utilizing

post-processing methods such as Hot Isostatic Pressing could potentially reduce PIM levels even further. Additionally, continued investigation into the relationship between PIM and AM-SLM will help to optimize the AM-SLM processes and materials, further minimizing PIM levels. Ongoing research is crucial to ensure that AM-SLM can be reliably used for the production of high-performance electromagnetic components across a wide range of advanced technological applications.

Chapter 6
Conclusions and Future Directions

This chapter serves to summarize the research project, present key findings, and offer insights into the outcomes. Section 6.1 discusses the conclusions drawn from the research. Section 6.2 outlines future directions and suggests areas for further investigation.

6.1 Conclusions

In this thesis, the primary objective was to explore the PIM performance of metal RF parts and how it is affected by metal 3D-printing, also known as AM-SLM. The thesis goal was to model a test object, likely to induce PIM, as well as a setup feasible to measure the PIM levels.

The study found that AM-SLM material exhibits tendencies to be worse in terms of PIM performance. The PIM is on average 5 dB. These results indicate that AM-SLM could be interesting as a manufacture method, though more research is necessary.

The findings have significant implications for the satellite and mobile industry. Specifically, they suggest that utilizing AM-SLM as a manufacture method would not significantly degrade the PIM performance of the product. This would allow for designs consisting of complex geometry, which is sought after within antenna, waveguide, and filter design. Further, this contributes to a deeper understanding of PIM sources and provides a foundation for further research to characterize the PIM in 3D-printed RD components.

Most other studies have focused on the mechanical properties when it comes to AM-SLM, such as the durability and structural integrity of the print. However, as far as this author's knowledge, no research has been done on the PIM levels in AM-SLM materials. The results do seem to go in line with the proposed theory, that an increase in the porosity of a material will increase the skin effect, which in turn increase surface currents and PIM.

Several limitations must be acknowledged. These include the metal printing quality provided by RISE, number of samples, and the equipment available on site. The printing quality could be improved by another machine or precision and post processing could be employed. These are likely to reduce the porosity in the print. Further, the setup was limited to the equipment available on site. This meant the setup had to be build where radiating horns were used, which added an uncertainty

of PIM coming from outside sources. These factors may have influenced the results and should be considered when interpreting the findings.

In conclusion, this research provides important insights into the PIM characterization of 3D-printed components. The results suggest that AM-SLM printed material does perform slightly worse than milled manufactured, however the increase in PIM level is low enough to suggest it could be a feasible method in satellite manufacturing. Ongoing research and development in this area are crucial for utilizing AM-SLM in large scale RF component manufacture.

6.2 Future Directions

Future research should focus on investigating the suggested setups mentioned, including the closed setup with diplexers and the development of the test object as interdigital or coaxial resonator filters. These setups would enhance the measurement accuracy by isolating PIM sources and ensuring that only the PIM from the test object itself is measured, making it a more reliable test method.

One key area for future investigation is exploring how post-processing methods, such as HIP, could influence the performance of AM-SLM printed components. Understanding the effects of HIP and other post-processing techniques on the PIM level of printed components could be an important step to using the manufacture method within the industry.

Additionally, research should aim to understand the relationship between PIM levels and surface area by printing and evaluating test objects of varying lengths. This would provide insights into how different geometries and sizes impact PIM performance, which is important for optimizing design and manufacturing processes.

It is crucial to emphasize that this is an emerging field, and further studies are needed to deepen our understanding. By continuing to explore these areas, the potential for improving the reliability and performance of AM-SLM printed components in electromagnetic applications can be significantly enhanced.

References

[1] H. J. Niu and T. H. Chang, "Instability of scan tracks of selective laser sintering of high speed steel powder," *Scripta Materialia*, vol. 41, no. 11, pp. 1229–1234, 1999.

[2] C. A. Balanis, *Antenna Theory: Analysis and Design*. Wiley, 2018.

[3] ASTM International, *Standard Terminology for Additive Manufacturing Technologies*, ASTM International Std., 2012, withdrawn 2023.

[4] "Ericsson mobility report," Ericsson AB, Tech. Rep., 2023.

[5] M. Mattsson, "Intermodulation distortion in active and passive components," Chalmers University of Technology Department of Microtechnology and Nanoscience - MC2, Tech. Rep., 2023.

[6] V. Pashintsev, M. Peskov, and V. Tsimbal, "Analysis of the causes of energy losses during processing of signals with frequency-selective fading and intersymbol interference," in *2020 22th International Conference on Digital Signal Processing and its Applications (DSPA)*, 2020, pp. 1–5.

[7] J. Pedro and B. Carvalho, *Intermodulation Distortion in Microwave and Wireless Circuits*. Norwood: Artech House, 2003.

[8] Z. Cai, L. Liu, F. de Paulis, and Y. Qi, "Passive intermodulation measurement: Challenges and solutions," *Engineering*, vol. 14, pp. 181–191, 2022.

[9] J. R. Wilkerson, P. G. Lam, K. G. Gard, and M. B. Steer, "Distributed passive intermodulation distortion on transmission lines," *IEEE Transactions on Microwave Theory and Techniques*, vol. 59, no. 5, pp. 1190–1205, 2011.

[10] D. Smacchia, P. Soto, V. E. Boria, M. Guglielmi, C. Carceller, J. Ruiz Garnica, J. Galdeano, and D. Raboso, "Advanced compact setups for passive intermodulation measurements of satellite hardware," *IEEE Transactions on Microwave Theory and Techniques*, vol. 66, no. 2, pp. 700–710, 2018.

[11] J. Boyhan, H. Henzing, and C. Koduru, "Satellite passive intermodulation: systems considerations," *IEEE Transactions on Aerospace and Electronic Systems*, vol. 32, no. 3, pp. 1058–1064, 1996.

[12] K. Cheng, M. Qu, J. Shi, and X. Tao, "Design of wideband omt choke flanges for low pim satellite communication applications," *IEEE Transactions on Electromagnetic Compatibility*, vol. 64, no. 4, pp. 1105–1111, 2022.

[13] "Why additive, why now?" Markforged, Tech. Rep., 2022.

[14] C. Vicente and H. L. Hartnagel, "Passive-intermodulation analysis between rough rectangular waveguide flanges," *IEEE Transactions on Microwave Theory and Techniques*, vol. 53, no. 8, pp. 2515 – 2525, 2005.

[15] C. Vicente, D. Wolk, H. L. Hartnagel, B. Gimeno, V. E. Boria, and D. Raboso, "Experimental analysis of passive intermodulation at waveguide flange bolted connections," *IEEE Transactions on Microwave Theory and Techniques*, vol. 55, no. 5, pp. 1018 – 1028, 2007.

[16] J. Henrie, A. Christianson, and W. J. Chappell, "Prediction of passive intermodulation from coaxial connectors in microwave networks," *IEEE Transactions on Microwave Theory and Techniques*, vol. 56, no. 1, pp. 209 – 216, 2008.

[17] Y. Yamamoto and N. Kuga, "Short-circuit transmission line method for pim evaluation of metallic materials," *IEEE Transactions on Electromagnetic Compatibility*, vol. 49, no. 3, pp. 682 – 688, 2007.

[18] G. Macchiarella, G. B. Stracca, and L. MiglioIi, "Experimental study of passive intermodulation in coaxial cavities for cellular base stations duplexers," in *34th European Microwave Conference*, Amsterdam, Netherlands, 2004, pp. 981–984.

[19] D. S. Kozlov, A. P. Shitvov, A. G. Schuchinsky, and M. B. Steer, "Passive intermodulation of analog and digital signals on transmission lines with distributed nonlinearities: Modelling and characterization," *IEEE Transactions on Microwave Theory and Techniques*, vol. 64, no. 5, pp. 1383–1395, 2016.

[20] Q. M. Khan and D. Kuylenstierna, "Analysis of Q-factor for AM-SLM cavity based resonators using surface roughness models," *IEEE Journal on Multiscale and Multiphysics Computational Techniques*, 2024.

[21] E. Brandl, U. Heckenberger, V. Holzinger, and D. Buchbinder, "Additive manufactured AlSi10Mg samples using selective laser melting (SLM): Microstructure, high cycle fatigue, and fracture behavior," *Materials & Design*, vol. 34, pp. 159–169, 2012.

[22] Z. Cai, L. Liu, F. de Paulis, and Y. Qi, "Passive intermodulation measurement: Challenges and solutions," *Engineering*, vol. 14, pp. 181–191, 2022.

[23] L. Huacheng, "Intermodulation distortion optimization strategy based on active negative feedback in ultra-wideband low-power amplifiers," in *2023 IEEE 6th International Conference on Information Systems and Computer Aided Education (ICISCAE)*, 2023, pp. 1006–1009.

[24] P. K. Chaturvedi, *Microwave, Radar RF Engineering.* Springer, 2018.

[25] J. Sanford, "Passive intermodulation considerations in antenna design," in *Proceedings of IEEE Antennas and Propagation Society International Symposium.* Ann Arbor, MI, USA: IEEE, June 28–July 2 1993, pp. 1651–1654.

[26] D. E. Zelenchuk, A. P. Shitvov, A. G. Schuchinsky, and V. F. Fusco, "Passive intermodulation in finite length of printed microstrip line," *IEEE Transactions on Microwave Theory and Techniques*, vol. 56, no. 11, pp. 2426–2434, 2008.

[27] 3GPP, "Passive intermodulation (PIM) handling for base stations (BS)," 3GPP, France, Tech. Rep. TR 37.808, 2013.

[28] G. Schennum and G. Rosati, "Minimizing passive intermodulation product generation in high power satellites," in *1996 IEEE Aerospace Applications Conference. Proceedings*, vol. 3, 1996, pp. 155–164 vol.3.

[29] R. Huang, L. Bi, J. Wu, Y. Jiang, Z. Zhou, W. Zhuang, and J. Luo, "A study of passive intermodulation of rf connectors in vibration environment," in *2021 4th International Conference on Advanced Electronic Materials, Computers and Software Engineering (AEMCSE)*, 2021, pp. 83–86.

[30] J. R. Wilkerson, K. G. Gard, and M. B. Steer, "Electro-thermal passive intermodulation distortion in microwave attenuators," in *2006 European Microwave Conference*, 2006, pp. 157–160.

[31] D. M. Pozar, *Microwave Engineering*, 4th ed. Wiley, 2012.

[32] S. Groiss, I. Bardi, O. Biro, K. Preis, and K. Richter, "Parameters of lossy cavity resonators calculated by the finite element method," *IEEE Transactions on Magnetics*, vol. 32, no. 3, pp. 894–897, May 1996.

[33] M. Holmberg *et al.*, "On surface losses in direct metal laser sintering printed millimeter and submillimeter waveguides," *J. Infrar. Millim. Teraher. Waves*, vol. 39, pp. 535–545, 2018.

[34] H. Nakajima, *Porous Metals with Directional Pores*, 1st ed. Springer Tokyo, 2013.

[35] R. Sorrentino and O. A. Peverini, "Additive manufacturing: a key enabling technology for next-generation microwave and millimeter-wave systems [point of view]," *Proceedings of the IEEE*, vol. 104, no. 7, pp. 1362–1366, 2016.

[36] "Executive summary - wholers world report 2023," Wholers Associated, Tech. Rep., 2023.

[37] J. Giannatsis and V. Dedoussis, "Additive fabrication technologies applied to medicine and health care: a review," *International Journal of Advanced Manufacturing Technology*, vol. 40, no. 1-2, pp. 116–127, 2009.

[38] E. Achilous and J. T. Czernuszka, "Making tissue engineering scaffolds work. review: the application of solid freeform fabrication technology to the production of tissue engineering scaffolds," *European Cells & Materials*, vol. 5, pp. 29–39, discussion 39–40, 2003.

[39] Y. Song, Y. Yan, R. Zhang, D. Xu, and F. Wang, "Manufacturing of the die of an automobile deck part based on rapid prototyping and rapid tooling technology," *Journal of Materials Processing Technology*, vol. 120, no. 1-3, pp. 237–242, 2002.

[40] C. L. Thomas, T. M. Gaffney, S. Kaza, and C. H. Lee, "Rapid prototyping of large scale aerospace structures," in *Proceedings of Aerospace Applications Conference IEEE*, vol. 4, Aspen, CO, 1996, pp. 219–230.

[41] E. D. Cullens, L. Ranzani, K. J. Vanhille, E. N. Grossman, N. Ehsan, and Z. Popovic, "Micro-fabricated 130–180 GHz frequency scanning waveguide arrays," *IEEE Trans. Antennas Propag.*, vol. 60, no. 8, pp. 3647–3653, August 2012.

[42] A. M. N. Ai-Mobin, R. Shankar, W. Cross, J. Kellar, K. W. Whites, and D. E. Anagnostou, "Advances in direct-write printing of RF-MEMS using M3D," in *IEEE MTT-S Int. Microw. Symp. Dig.*, June 2014, pp. 1–6.

[43] E. C. Santos, M. Shiomi, K. Osakada, and T. Laoui, "Rapid manufacturing of metal components by laser forming," *International Journal of Machine Tools and Manufacture*, vol. 46, no. 12–13, pp. 1459–1468, 2006.

[44] I. Sokol. (2014) 3D-printed aluminum antenna support may be space-bound. [Online]. Available: https://www.mwrf.com/technologies/components/passive-components/article/21845990/3d-printed-aluminum-antenna-support-may-be-space-bound

[45] L. Griffiths. (2015) Airbus division 3D prints aluminium component for Eurostar E3000 satellite. [Online]. Available: https://www.tctmagazine.com/additive-manufacturing-3d-printing-news/airbus-division-3d-prints-aluminium-components-for-new-eurostar-satellite/

[46] F. Calignano, D. Manfredi, E. P. Ambrosio, S. Biamino, M. Lombardi, E. Atzeni, A. Salmi, P. Minetola, L. Iuliano, and P. Fino, "Overview on additive manufacturing technologies," *Proceedings of the IEEE*, vol. 105, no. 4, pp. 593–612, 2017.

[47] T. Kurzynowski, E. Chlebus, B. Kuźnicka, and J. Reiner, "Parameters in selective laser melting for processing metallic powders," *Proc. SPIE*, vol. 8239, p. 823914, Feb 2012.

[48] B. Leutenecker-Twelsiek, C. Klahn, and M. Meboldt, "Considering part orientation in design for additive manufacturing," *Procedia CIRP*, vol. 50, pp. 408–413, 2016.

[49] M. Van Elsen, "Complexity of selective laser melting: a new optimisation approach," Ph.D. dissertation, Katholieke Universiteit Leuven, 2007.

[50] K. C. A. B. U. P. Manfredi, Calignano and Fino, "Additive manufacturing of Al alloys and Aluminium Matrix Composites (AMCs)," in *Light Metal Alloys Applications*. InTech, Jun. 2014.

[51] E. O. Olakanmi, "Selective laser sintering/melting (SLS/SLM) of pure Al, Al–Mg, and Al–Si powders: Effect of processing conditions and powder properties," *Journal of Materials Processing Technology*, vol. 213, pp. 1387–1405, 2013.

[52] F. Calignano, "Design optimization of supports for overhanging structures in aluminum and titanium alloys by selective laser melting," *Materials & Design*, vol. 64, pp. 203–213, 2014.

[53] H. V. Atkinson and S. Davies, "Fundamental aspects of hot isostatic pressing: An overview," *Metallurgical and Materials Transactions A*, vol. 31, pp. 2981–3000, 2000.

[54] N. L. Loh and K. Y. Sia, "An overview of hot isostatic pressing," *Journal of Materials Processing Technology*, vol. 30, pp. 45–65, 1992.

[55] Z. Yuan, A. Chen, L. Xue, R. Ma, J. Bai, J. Zheng, X. Bai, J. Zheng, S. Mu, and L. Zhang, "Effect of hot isostatic pressing and heat treatment on the evolution of precipitated phase and mechanical properties of GH3230 superalloy fabricated via selective laser melting," *Journal of Materials Research and Technology*, vol. 30, pp. 507–519, 2024.

[56] "Minimizing PIM generation from RF cables and connectors," Santron, Tech. Rep., 2012.

[57] W. A. Imbriale, S. S. Gao, and L. Boccia, *Space Antenna Handbook*. Wiley Telecom, 2012.

[58] D. Bond, C. S. Guenzer, and C. A. Carosella, "Intermodulation generation by electron tunneling through aluminum oxide films," *Proceedings of the IEEE*, vol. 67, no. 12, pp. 1643–1652, 1979.

[59] M. Javadi and M. Tajdari, "Experimental investigation of the friction coefficient between aluminium and steel," *Materials Science- Poland*, vol. 24, 01 2006.

[60] V. Patel, R. Kant, A. Choudhary, M. Painuly, and S. Bhattacharya, "Performance characterization of Bi2O3/Al nanoenergetics blasted micro-forming system," *Defence Technology*, vol. 15, 07 2019.

Appendix A

Appendix A: Blueprints of Designed Components

The following appendix contain the blueprints of the designed and manufactured parts. The cavities in the components have all been designed and tested in HFSS. After the cavities were achieved desirable functionality, the cavities where modeled in CAD to be encased in metal.

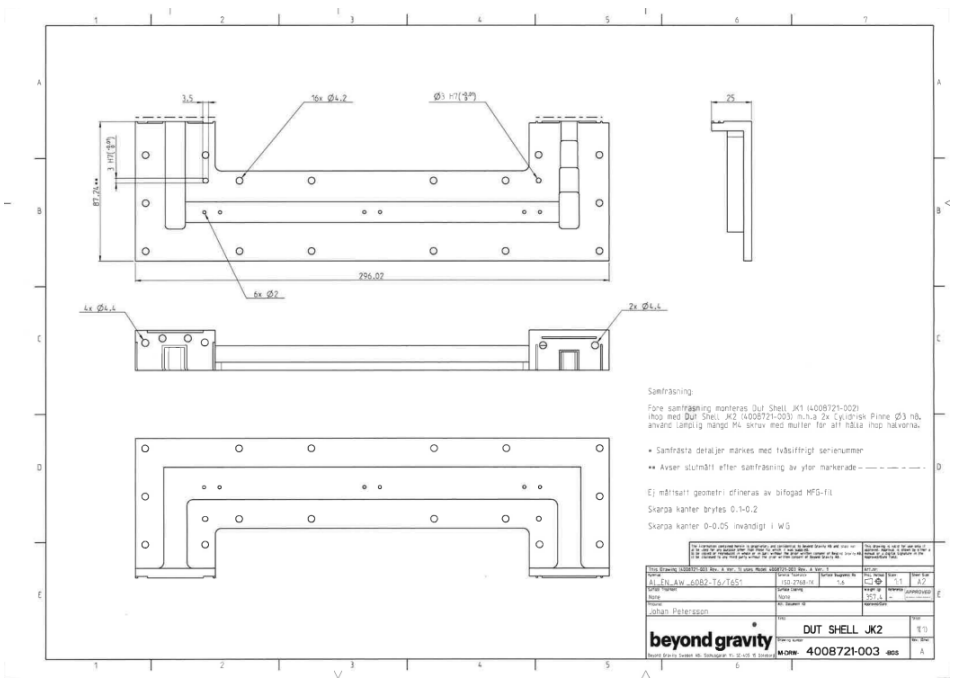

Figure A.1: Blueprint of the DUT shell, showing one side.

Fig. A.1 and Fig. A.2 show the blueprint of the DUT. The blueprint show the channel. The channel contain small holes to attach Ultem plastic support pieces, see Fig. A.3, to hold the sample in place.

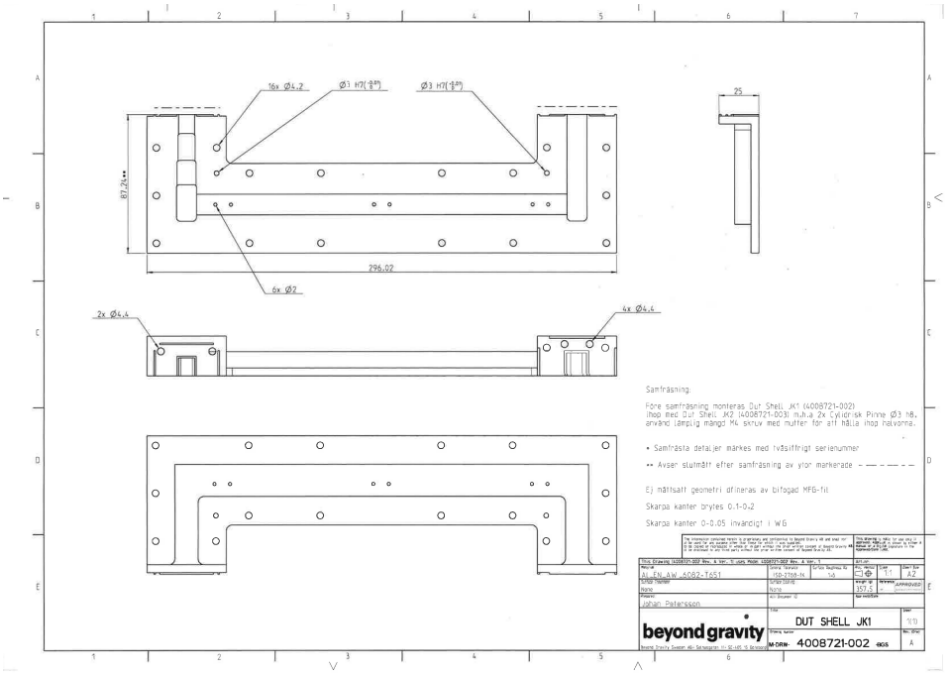

Figure A.2: Blueprint of the DUT shell, showing the other connecting side.

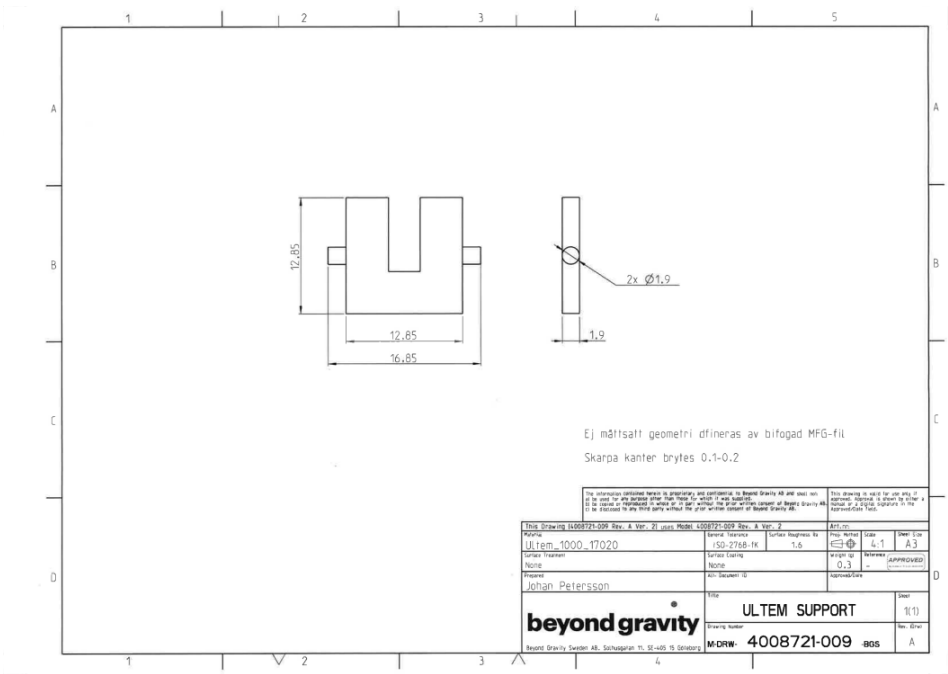

Figure A.3: Blueprint of the ULTEM support pieces.

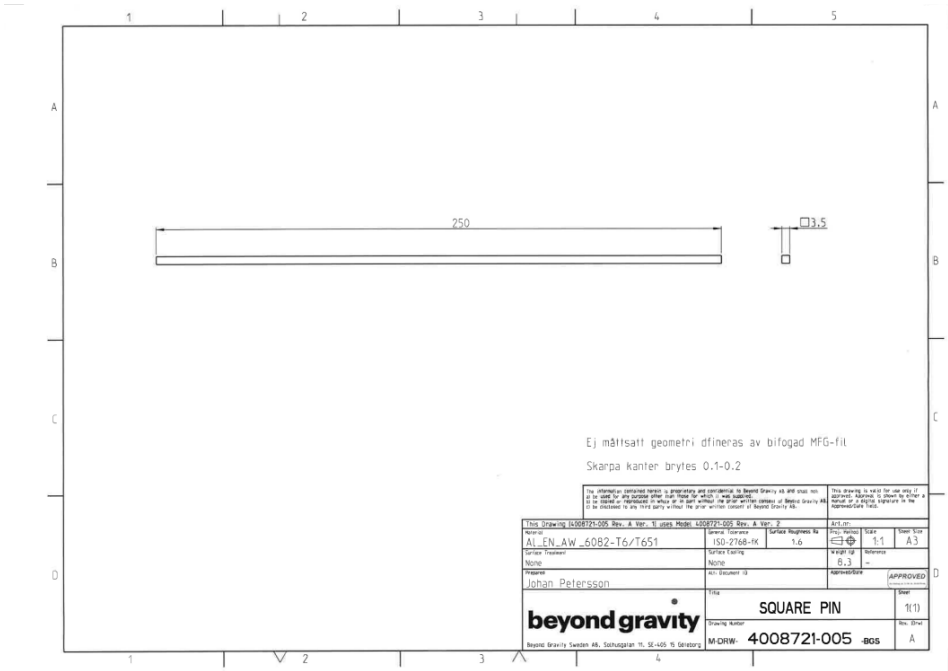

Figure A.4: Blueprint of the square pin test sample.

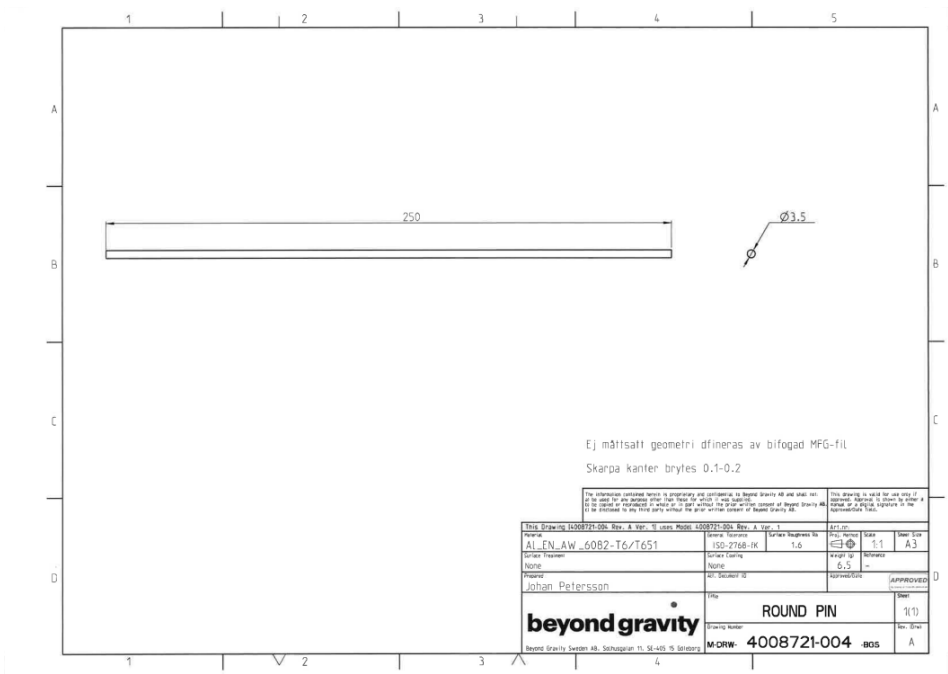

Figure A.5: Blueprint of the round pin test sample.

Fig. A.5 and Fig. A.4 show the metal samples inserted into the channel of the DUT displayed in Fig. A.1. The samples are equal length, one has a squared cross section and the other a circular cross section.

In Fig. A.6 the blueprint of the TX filter is shown. The filter is designed to have a high isolation at the desired frequencies. The high pressure interfaces can be seen around the opening of the waveguide. In Fig. A.7 the blueprint of the RX highpass transformer is shown. In Fig. A.8 the blueprint of a waveguide connecting two filters are shown.

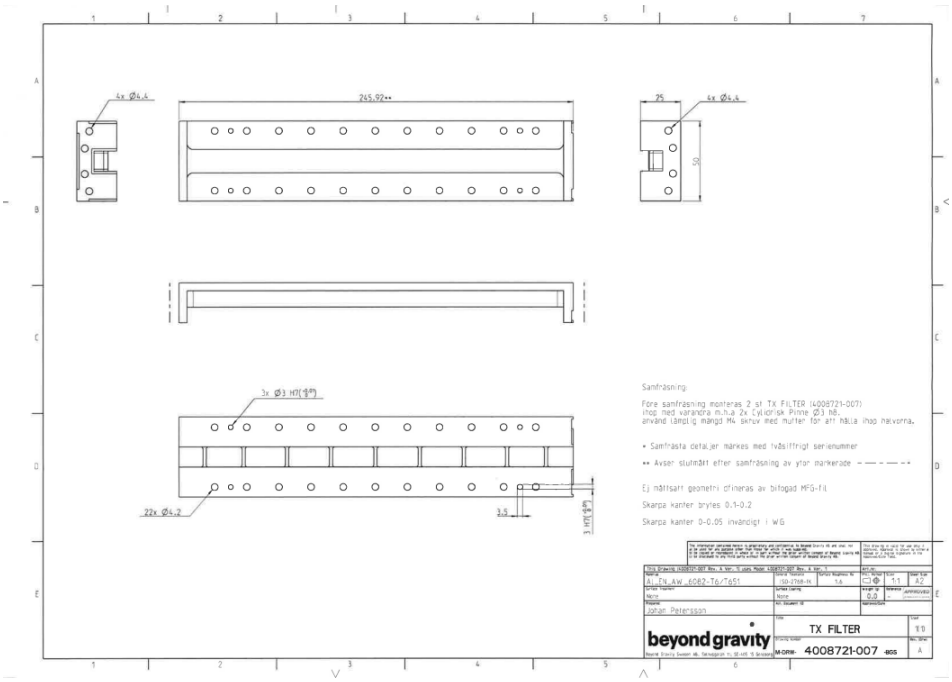

Figure A.6: Blueprint of the TX filter.

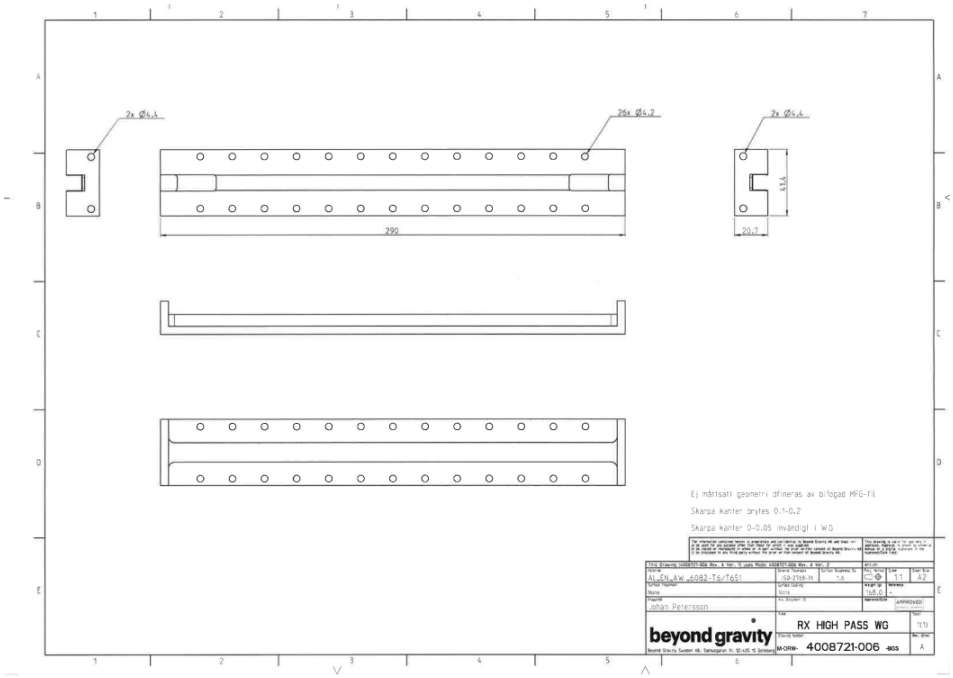

Figure A.7: Blueprint of the TX filter.

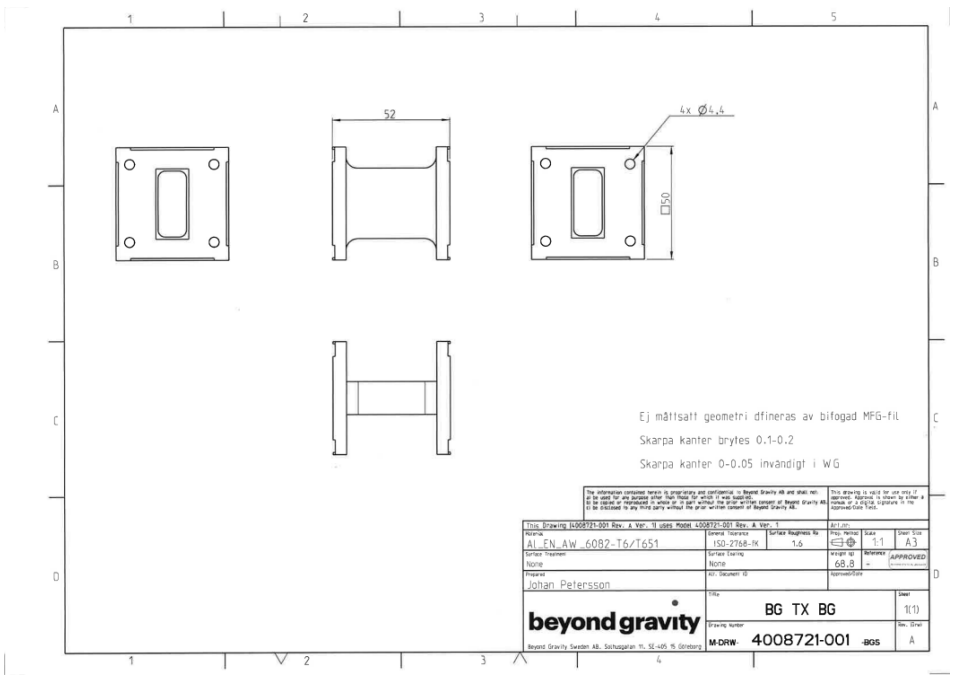

Figure A.8: Blueprint of waveguide transition between two TX filters.

Printed by Tryckeriet i E-huset, Lund 2024

LUND
UNIVERSITY

Series of Master´s theses
Department of Electrical and Information Technology
LU/LTH-EIT 2024-984
http://www.eit.lth.se